R022-A

Application of Solar Soaring Power Manager (Phase I)
Submitted by Packet Digital

Response to Reviewers
Prepared by Packet Digital and Robert Walters of the Naval Research Lab

1. **The objectives or goals of the proposed project with respect to clarity and consistency with North Dakota Industrial Commission/Renewable Energy Council goals**

Response to Reviewer 1B: The reviewer makes a good point that our description of the modeling effort did not specifically refer to the North Dakota environment, but instead to the general environment of a UAV. Given the North Dakota focus of this proposal, it would make sense to design the solar cell specifically for the known solar insolation profile for North Dakota. The strength of the NRL modeling is that the specific environment can be used in terms of the typical solar spectrum and intensity to design the solar cell. NRL has extensive experience in using the NASA and NREL environment modeling databases and simulation codes to generate the required environmental data. Furthermore, the proposed multi-junction (MJ) solar cell design naturally lends itself to optimization for a given illumination spectrum and intensity level. Therefore, the proposed program provides an excellent opportunity to accurately model the solar cell design specifically for the North Dakota agricultural and pipeline environment and to build the solar cell using the transfer-printing technique.

This project will include ComDel Innovations and bring manufacturing to the region, as well as involve UND, NDSU, and the Northern Plains Unmanned Systems Test Site.

2. **With the approach suggested and time and budget available, the objectives are ...**

Response to Reviewer 1B: The reviewer provides a good summary here with what appears to be a positive assessment; however, only gives a rating of "3".

Response to Reviewer 1D: The reviewer is correct that it will be challenging to attain 40% within this program; however, our current technical results do suggest that our stated goals are achievable. While not described in the proposal, NRL has performed extensive modeling of materials to be used in stacked MJ devices. This modeling has presently focused on InP-based materials, with our latest results being presented this past June at the IEEE Photovoltaic Specialist Conference (PVSC). A copy of the conference proceedings is included here. As shown in the paper, we have successfully stacked a three junction cell onto a single junction cell, and the resulting device displayed an efficiency of 34.5% under one sun conditions. We feel that this positions us very well for executing the proposed program.

Phase I involves creation of a 30-35% efficient panel leveraging current research and development efforts. 40% efficient solar *cells* will be delivered at the end of Phase II and 40% efficient *panels* will be delivered at the end of Phase III.

The reviewer also refers to the fact that the best solar cell efficiencies have been achieved only on small area, ridged solar cells, which may suggest a challenge in obtaining similar efficiencies

with flexible cells. While the reviewer makes a good point, the transfer-printing process will mitigate this risk. As briefly described in the PVSC paper, the transfer-printing process creates small solar cell "chiplets". Therefore, we will be working with small area, rigid solar cells, so we will have an excellent chance of maintaining the "hero-cell" efficiency in our assembled panels. The flexibility is attained by transfer-printing the stacked solar cell onto a flexible substrate. In this way, a flexible array is formed from rigid solar cells. Such transfer-printing of semiconductor chips onto flexible substrates has been demonstrated by the University of Illinois at Urbana-Champaign (UIUC) in the laboratory setting and commercially by MC-10 in Boston and Semprius in North Carolina.

3. **The quality of the methodology displayed in the proposal is ...**

Response to Reviewer 1B: The reviewer is correct in this assessment. The fact is that this proposal does not address the payload to any great extent, and as a result, the processor design and development did not specifically include payload control, sense-and-avoid features, and traditional navigation functionality. This is the case because the funding level available within this program was not sufficient to include that level of complexity. The focus of this proposal is to demonstrate the key, new technologies that will enable persistent flight of a small UAV without the need of fuel. With these key, enabling technologies demonstrated, namely efficient power electronics, auto-soaring, and high efficiency, flexible PV, the incorporation of additional functions will be straightforward since such systems currently exist for UAV platforms.

The sizing (compute power, memory, etc.) of our microprocessor will account for the other tasks mentioned, such as avoidance and flight plan management. Ample headroom will be provided in our microprocessor selection to account for "normal" flight management tasks, based on existing UAV component designs and functionality, in addition to our power management and soaring features. The precise details of the microprocessor capabilities will be determined in the requirements capture phase of the project.

A fixed wing aircraft was selected for this project based on applicability to agricultural applications as well as interest from DoD customers. Some of the technologies may transfer to other types of aircraft as well, such as using the solar panels on a lighter-than-air vehicle and utilizing the power electronics in quad/hexa/octo-copter vehicles. These applications will be investigated in later phases of the project.

Response to Reviewer 1D: We agree that there was only limited technical detail included in the proposal. This is the case simply due to space limitations. We can now quickly summarize the key challenges for the solar cell development to be achieving high enough material quality in the semiconductor growth to give high enough PV performance to achieve the desired 40% efficiency. We consider this to be only a moderate risk as we have extensive experience with growth of high quality, multi-layered, highly complicated optoelectronic devices as evidenced by some of our IR detector work (E. H. Aifer Appl. Phys. Lett. 89, 053519 (2006); doi: 10.1063/1.2335509- See document attached) as well as our solar cell work. There is ~~also~~ risk in assembling the stacked solar cells in a flexible array. This is a high risk since there is only limited examples of this in the past. We mitigate this risk through our close collaboration with the original inventors of the transfer-printing technique at UIUC (two graduates from the UIUC team now work at NRL). Furthermore, we are working closely with the two commercial companies

employing the transfer-printing technique, Semprius and MC-10, both of whom have produced flexible solar panels.

4. **The scientific and/or technical contribution of the proposed work to specifically address North Dakota Industrial Commission/Renewable Energy Council goals will likely be ...**

Response to Reviewer 1D: Regarding UAV cost, the technologies to be added to the UAV will not be expensive compared to the sensor payload. The solar arrays will have costs associated with them, but the transfer-printing process allows for low cost manufacturing since it allows for reusing the semiconductor substrate, which accounts for nearly half of the solar cell cost.

~~Also~~ Furthermore, it is worth noting that the solar cells developed in this project can also be used in the concentrated solar panel technology being sold by Semprius. Therefore, while this project seeks to capitalize on the unique properties of transfer-printing to create an extremely high efficiency solar cell as a UAV power source, the solar cell technology is also directly applicable to large area, terrestrial power plants.

This project will support 20-25 jobs. Successful completion of this project could enable many more applications for UASs. Today's applications are only the tip of the iceberg. Upon successful completion even more jobs could be a possibility.

5. **The principal investigator's awareness of current research activity and published literature as evidenced by literature referenced and its interpretation, and by the reference to unpublished research related to the proposal is:**

Response to Review 1B: The reviewer is correct that efficiencies about 40% have been published, but all of these were measured under concentration. We will be making all of our measurements under one sun conditions. In addition to the growth and fabrication facilities, NRL maintains a complete solar cell measurement and characterization laboratory, and all of the performance measurements will be made according to industry standards.

Response to Review 1D: We apologize for not including more references. When referring to "the most advanced cell" demonstrating 33%, we were referring to the high efficiency, large area, flexible solar cell that has been demonstrated by Microlink Devices in Chicago and Emcore Photovoltaics in Albuquerque. A reference to work that we have done with Microlink is: Trautz et al. "Mobile Solar Power", IEEE JOURNAL OF PHOTOVOLTAICS, VOL. 3, NO. 1, JANUARY 2013. Attached.

6. **The background of the investigator(s) as related to the proposed work**

Response to Reviewer 1D: In response to the reviewer's comments, it appears that available information from the Internet has established NRL's background and experience in MJ solar cells. To add some specific references, please see the following publications:

- Lumb et al. "Double quantum-well tunnel junctions with high peak tunnel currents and low absorption for InP multi-junction solar cells", Appl. Phys. Lett. 100, 213907 (2012); doi: 10.1063/1.4722890

- Lumb, et. al, "Quantum wells and superlattices for III-V photovoltaics and photodetectors". Presented at the SPIE Solar Energy + Technology, SPIE. (Vol. 8471, pp. 84710A–84710A–10). doi:10.1117/12.964654
- Schmieder, et al. "Analysis of GaAs Solar Cells at High MOCVD Growth Rates." Proc. 40th IEEE Photovoltaic Specialist Conference, Denver, CO, June 2014.

Also, we believe that our response to Item 2 has provided further evidence of NRL's level of experience with the stacked MJ devices. While NRL has yet to demonstrate a 6J device, their present experience level positions them very well to achieve this.

7. **The project management plan, including a well-defined milestone chart, schedule, financial plan, and plan for communications among the investigators and subcontractors.**

Response to Reviewer 1B: While the reviewer is correct that the solar insolation will change with season, it is not practical to consider a solar cell optimized for each season. With the nature of solar cell manufacturing and the fact that this will be a relatively low volume solar cell to manufacture, it would not be economically feasible to considered producing more than one solar cell design. Therefore, our plan is to use our modeling to determine the best design to encompass the broadest operational environment as possible. Therefore, testing in various seasons would be ideal if time and funding allows, and testing in a single season will provide sufficient test data.

Response to Reviewer 1D: The reviewer commented that it would be better if the solar cell modeling and development would begin immediately at the start of the program instead of one month in, as stated in our schedule. We agree, and we can assure the reviewer that NRL is working on this at this very moment, as part of internal NRL efforts so that we will "hit the ground running" at the start of the program.

Battery selection is part of the materials acquisition and is scheduled for the very beginning of the project.

10. **The proposed budget "value" relative to the outlined work and the financial commitment from other sources**

Response to Reviewer 1D: The reviewer commented that we are only meeting the minimum requirement of 50% cost sharing. The NRL and their partner manufacturer are utilizing additional financing to develop the solar cells for other applications and will be leveraging existing work on the manufacturing techniques for highly efficient flexible multi-junction solar cells. These are not accounted for in the budget but represent significant external funding contributions as well as a head start on the development effort.

Mobile Solar Power

Kelly M. Trautz, Phillip P. Jenkins, Robert J. Walters, David Scheiman, Raymond Hoheisel, Rao Tatavarti, Ray Chan, Haruki Miyamoto, Jessica G. J. Adams, Victor C. Elarde, and James Grimsley

***Abstract*—The military's need to reduce both fuel and battery resupply is a real-time requirement for increasing combat effectiveness and decreasing vulnerability. Mobile photovoltaics (PV) is a technology that can address these needs by leveraging emerging, flexible space PV technology. In this project, the development and production of a semirigid, lightweight, efficient solar blanket with the ability to mount on, or stow in, a backpack and recharge a high-capacity rechargeable lithium-ion battery was undertaken. The 19% efficient blanket consists of a 10 × 3 solar array of 20 cm^2 and single-junction epitaxial lift-off solar cells, which have an efficiency of ~22% under AM1.5G illumination. A power-conditioning module was also developed to interface the solar panel to the battery. Thirteen systems were outfitted during a Limited Objective Experiment-1 in February 2012, and based on the results, a second version of the system is in development.**

***Index Terms*—Battery recharger, epitaxial lift off, solar cell, solar panel.**

I. Introduction

ONE of the most significant challenges currently facing the United States Marine Corps (USMC) is the need to supply sufficient electricity to individual Marines in a forward operating base (FOB), while reducing the number of batteries used and decreasing reliance on the logistics chain for liquid fuels. It is recognized that photovoltaic (PV) is the only renewable energy source that can meet this challenge. To fully meet the USMC power demands, these PV power systems must provide superior performance in terms of power generation both per unit mass (W/kg) and per unit area (W/m^2) compared with what is currently deployed.

The Mobile Solar Power (MSP) development project has leveraged existing PV technologies and expertise to make an immediate impact on the requirements of the USMC Energy Expeditionary Office (E2O). The U.S. Naval Research Laboratory (NRL), in collaboration with Microlink Devices, Inc., and Design Intelligence, Inc., has taken advantage of significant advances recently made in PV for space and concentrator PV (CPV) applications and has adapted these technologies to meet the requirements of the individual Marine. In particular, flexible solar cells with light to electricity conversion efficiency as high as 30% have been demonstrated in multicell panels [1]. This represents a potential 10× improvement in efficiency over existing thin-film solar technologies. By leveraging these technology breakthroughs, prototype MSP systems were developed and produced consisting of an array of solar cells packaged in a lightweight, semirigid unit that includes all power electronics necessary for battery recharging that can easily be integrated with the warfighter's equipment.

Fig. 1. Active solar-cell wafer removed from the growth substrate to form two flexible devices.

II. Solar Panel Development

In developing the solar panel, the cells had to be configured to fit within the Marine's available space constraints while still meeting power requirements and maintaining reliability.

A. Solar Cell Technology

For applications such as battery charging, it is desirable to maximize energy generation. While triple- and dual-junction cells have higher efficiencies than single-junction (SJ) cells, there were many system-related factors to optimize. Therefore, SJ gallium arsenide (GaAs) cells, while not having the highest efficiency, were applicable to understand the system-related issues, such as reliability, durability, and form factor, and were also less expensive to procure.

The SJ GaAs solar cells used in this project were formed by an epitaxial lift-off (ELO) process [2]. The ELO process removes the active solar cell layers from the rigid growth substrate, yielding a high efficiency, lightweight, flexible solar cell (see Fig. 1).

Manuscript received May 23, 2012; revised August 15, 2012; accepted August 21, 2012. Date of publication September 12, 2012; date of current version December 19, 2012. This work was supported in part by the Energy Expeditionary Office, Office of Naval Research, and the Defense Advanced Research Projects Agency, in collaboration with MicroLink Devices, Inc., and Design Intelligence, Inc.

K. M. Trautz, P. P. Jenkins, R. J. Walters, and D. Scheiman are with the U.S. Naval Research Laboratory, Washington, DC 20375 USA (e-mail: Kelly.Trautz@nrl.navy.mil; phillip.jenkins@nrl.navy.mil; robert.walters@nrl.navy.mil; david.scheiman@nrl.navy.mil).

R. Hoheisel is with the U.S. Naval Research Laboratory and George Washington University, Washington, DC 20375 USA (e-mail: raymond.hoheisel.ctr.gm@nrl.navy.mil).

R. Tatavarti, R. Chan, H. Miyamoto, J. G. J. Adams, and V. C. Elarde are with MicroLink Devices, Inc., Niles, IL 60714 USA (e-mail: rtatavarti@mldevices.com; rchan@mldevices.com; hmiyamoto@mldevices.com; jadams@mldevices.com; velarde@mldevices.com).

J. Grimsley is with Digital Intelligence, Inc., LLC, Norman, OK 73019 USA (e-mail: grimsleyj@dii1.com).

Color versions of one or more of the figures in this paper are available online at http://ieeexplore.ieee.org.

Digital Object Identifier 10.1109/JPHOTOV.2012.2215580

2156-3381/$31.00 © 2012 IEEE

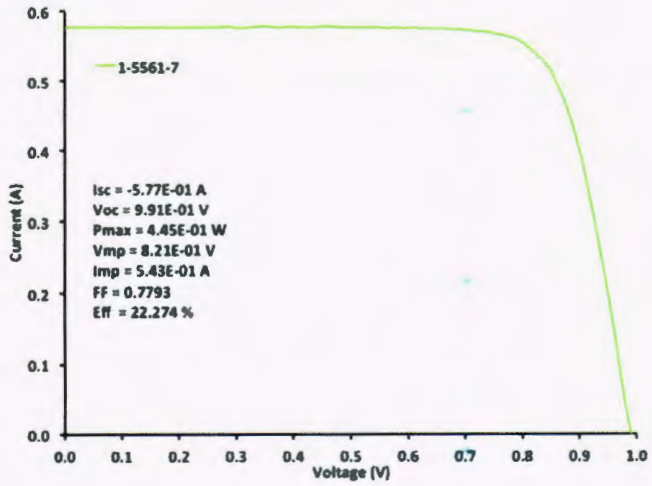

Fig. 2. Typical measured *I–V* curve of the MSP solar cells. The cell efficiencies ranged from 20 to 23%.

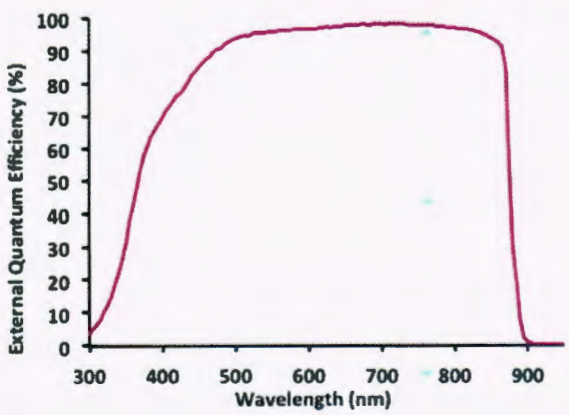

Fig. 3. Typical external quantum efficiency curves measured on SJ GaAs solar cells for MSP.

The SJ GaAs solar cells used in the MSP panels were 4 cm × 5 cm and had efficiencies ranging from ~20 to 23%. (see current versus voltage $(I - -V)$ measurement data in Fig. 2 and quantum efficiency in Fig. 3). The MSP cells produced, on average, ~500 mA (25 mA/cm^2) at short circuit, 0.98 V at open circuit, and 440 mW (22 mW/cm^2) at the maximum power point under AM1.5G illumination.

The ELO technology used in MicroLink's solar cells results in physically flexible cells, which allows the manufacture of a flexible MSP. ELO technology also allows the manufacture of low-cost cells because the substrates on which the cells are grown can be reused multiple times.

B. Solar Panel Design

Each MSP panel consists of 30 GaAs solar cells connected in series. Due to the conditions likely to be encountered in the field, it is necessary that the packaging of the solar panel be robust and rugged. To accomplish this, each array of solar cells was laminated between two sheets of transparent fluoropolymer film. The laminated cell array was then attached using adhesive

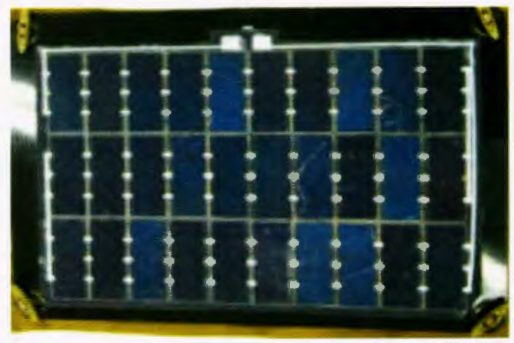

Fig. 4. MSP panel.

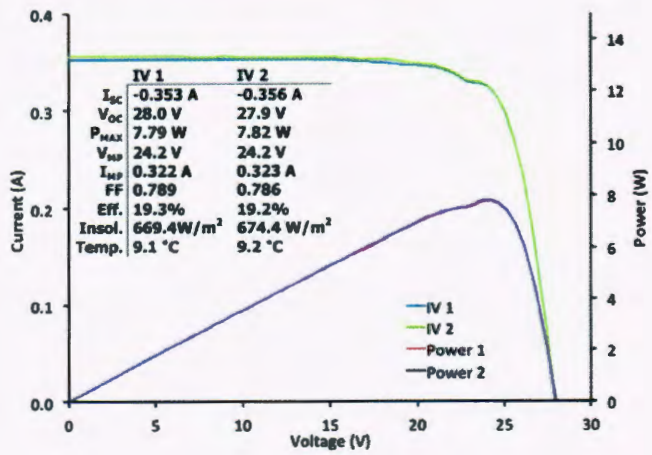

Fig. 5. Outdoor measurements of MSP panels.

to a thick, semirigid sheet of black plastic, which provided the stiffness necessary to protect the cells.

The panels will be exposed to external factors that could limit or eliminate cell performance such as damage from combat, partial shading, mishandling, etc. To ensure that the remaining connected cells continued to perform optimally, there were two redundant interconnects between each cell consisting of welded tabs, one of which was redundant, and a third silicon-based Schottky bypass diode.

The size and configuration of the solar panel were driven by the size of an average Marine backpack. Given a maximum space of 10.5 in × 17.5 in the panel design consists of a 30-solar-cell array that is 10.25 in × 15.5 in in size and 270 g in weight (see Fig. 4). A typical outdoor measurement of an MSP panel is shown in Fig. 5 demonstrating about 19% efficiency. *I–V*1 and *I–V*2 both show about 13 W under 1-sun AM1.5G illumination (right axis).

III. Modeling, Simulation, and Characterization

To determine a baseline and expectations for the systems performance during the Limited Objective Experiment-1 (LOE-1), modeling, and characterization were performed to estimate the electrical output of the SJ GaAs panels at Fort Pickett, VA, in February 2012.

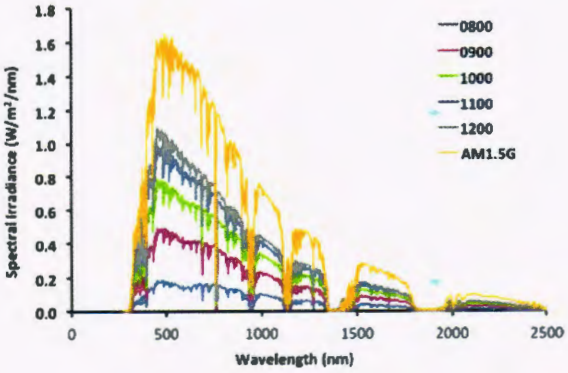

Fig. 6. Spectral simulation from SMARTS for the Fort Pickett location in Virginia on February 1, 2012. Spectra for various times of day are shown (times given in the legend), as well as the AM1.5G spectrum.

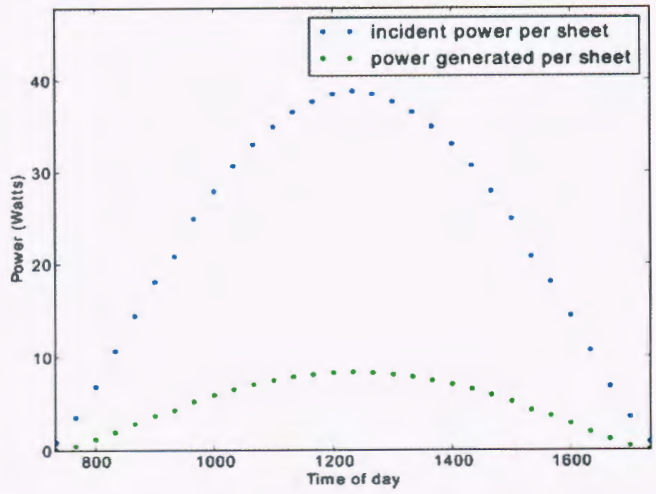

Fig. 7. Modeled performance of the MSP panels as a function of time throughout one day at Fort Pickett, VA, on February 1, 2012.

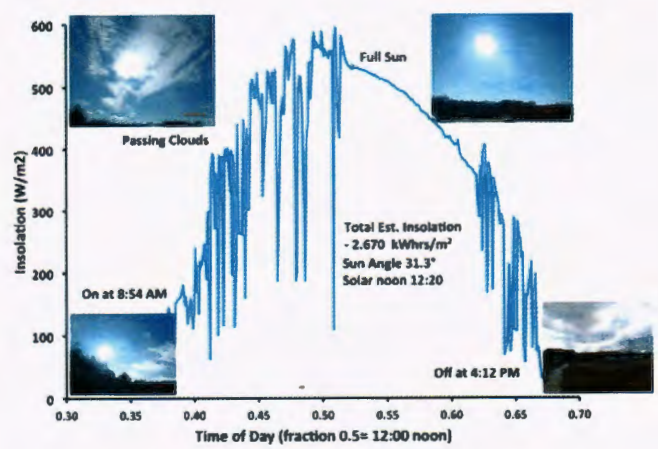

Fig. 8. Solar insolation measured at Fort Pickett during the day on January 12, 2012.

A. Solar Panel Modeling and Simulation

Prior to the LOE-1, modeling was performed to predict the performance of the MSP solar panels. Using a reliable, relevant spectral simulation from the SMARTS program [3] under specific operating conditions (location, season, weather, and duration), a performance model for the solar panel was developed. The approach taken utilizes an atmospheric radiative transfer model to simulate spectral conditions for a specific location (latitude and longitude) and date with appropriate inputs. Fig. 6 shows such a spectral simulation for average conditions at Fort Pickett on February 1, 2012. The spectra are seen to vary in both intensity and distribution across the day, and the data vary symmetrically from sunrise to sunset symmetric around 12:20 P.M. The total global insolation was 4.0 kWh/m^2/day. It should be noted that the spectra shown here is for a clear sky and does not include shading likely to occur from tree cover.

The SMARTS model provides an estimate of the solar input for the given location at the given time. Using the obtained spectral data, further modeling was performed to determine the expected power generation from the panel. The performance data from the MSP solar cells were calculated with a total cell area of 0.06 m^2 and the assumption that the panel lies flat on the ground. The data shown in Fig. 7 display power produced throughout the day. These results predict a maximum power generation of about 10 W per panel, total energy yield of one MSP panel of 50 Wh/day, and a peak panel efficiency of 21.5% at 12:20 P.M. with an average efficiency over daylight hours of 20.9%.

B. Solar Panel Characterization

Actual data were taken during a performance test at Fort Pickett on January 12, 2012, to verify the modeling and simulation data. During this test, the total solar insolation was measured along with the solar spectrum throughout the day using a precision spectral pyranometer and normal incidence pyrheliometer. The output of one MSP panel was measured in both horizontal and solar tracking configurations. The solar insolation is shown in Fig. 8, and the total insolation was about 2.7 kWh/m^2. This compares reasonably well with the SMARTS modeling value of 4.0 kWh/m^2 presented earlier when considering partial cloud cover during the day.

Fig. 9 shows the panel output power as a function of time. The continuous green line displays the power output when the panel was flat against a horizontal surface; drops in the power are attributed to cloud coverage. The red dots represent data measured when the panel was actively pointed directly at the sun. Typical *I–V* curves measured on this panel throughout the day in both the flat and solar-tracking configurations are shown in Fig. 10. The total power produced by the panel in the flat configuration was 30.1 Wh, giving a nominal efficiency of 18.7% (calculated using the cell area). This compares well with the modeled data shown in Fig. 7. The measured data are marginally less than the modeled data because the assembled panel has a lower efficiency compared with an individual cell (~18% compared with ~22%) due to resistive losses and slight cell mismatch.

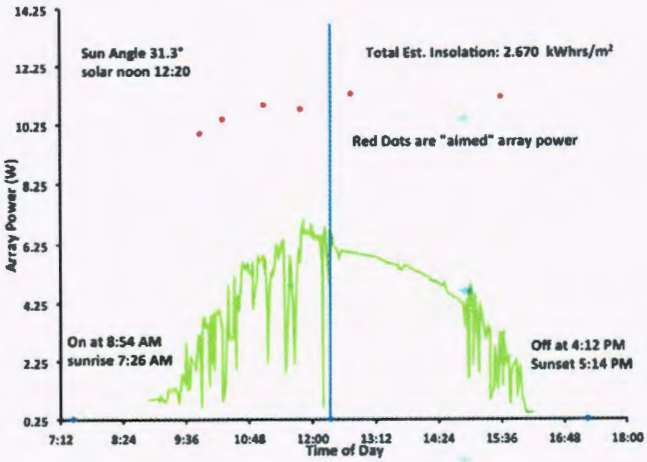

Fig. 9. Power output measured from MSP # 6 in both a flat and solar-tracking configuration during testing at Fort Pickett, VA, on January 12, 2012.

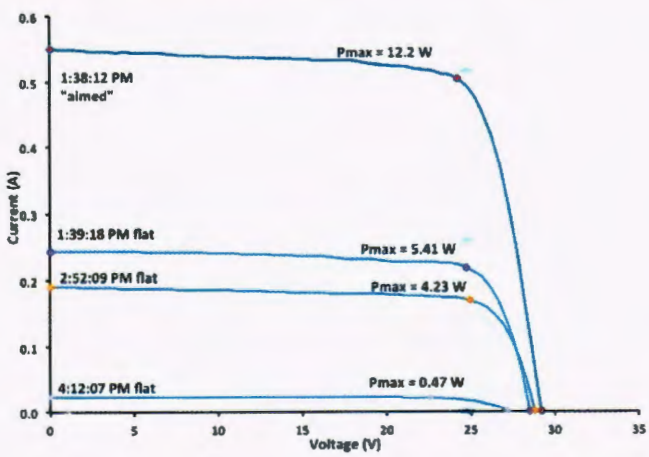

Fig. 10. *I–V* curves measured from MSP panel #6 during testing at Fort Pickett on January 12, 2012. The panel was placed horizontal, and curves measured at various times of the day are shown. The curve labeled "aimed" was angled to provide normal incidence illumination.

IV. System Interface Design

A. Power Control Electronics

A custom-designed circuit was built to interface the MSP solar panel to the BB-2590 to provide power management, maximum power point tracking (MPPT), and battery charge management. MPPT refers to adjusting the load placed on the solar panel so that power extracted is close to the maximum power point. The power control circuit uses the MPPT and adjusts the output voltage to match the BB-2590 lithium ion battery [4] input using either a buck or boost dc to dc circuit, and regulates the input current to charge the battery. The circuit was designed for a 15-W solar panel producing 28 V at open circuit and 23 V at maximum power. The maximum input voltage was 34 V, minimum of 10 V, with an optimal input voltage range of 23–28 V.

The charge control circuit was housed within a standard BB-2590 battery connector and held in place on the battery with a Velcro strap. The connector box and the battery are housed in a 100-round ammunition pouch that can be connected using modular lightweight load-carrying equipment (MOLLE) design [5] webbing. Fig. 11 shows the charging unit, attached to a BB-2590 (shown) and a solar panel (not shown), with a solid amber LED signifying that the panel is charging the battery in a nominal mode. The entire MSP system is depicted in Fig. 12.

Fig. 11. A BB-2590 with the MSP charge control circuit connector attached.

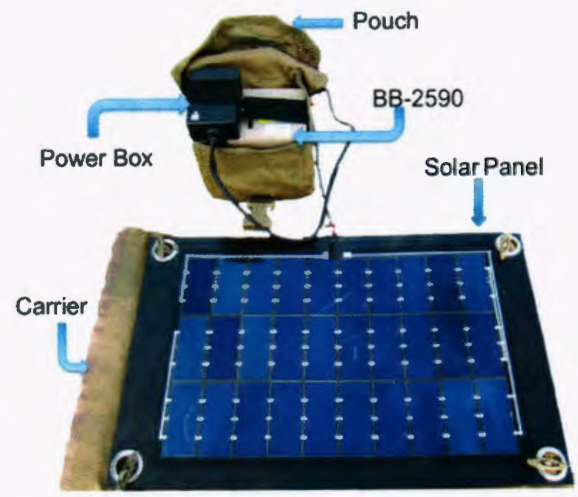

Fig. 12. MSP system components.

B. System Packaging

In order for the MSP to interface with the Marine backpack, a carrier was designed by USMC Gruntworks Squad Integration Facility using MOLLE. This carrier also serves as a protective case for the MSP when it is not in use. The panel can be attached to the outside of the carrier with Velcro and toggles. When not in use, the panel can be removed and stored inside the carrier or securely covered up with a flap. Fig. 13 shows several views of the carrier with and without the panel.

V. System Deployment

A. Limited Objective Experiment -1 (LOE-1) Test Plan

Thirteen MSP systems were outfitted for four days during the February 2012 LOE-1. Six Marines wore the system for the sole purpose of recharging BB-2590 batteries. During set intervals, the batteries' state of charge was evaluated. Four other Marines wore the systems along with two BB-2590s. This group charged one battery via the MSP, while using the other battery to operate their radio.

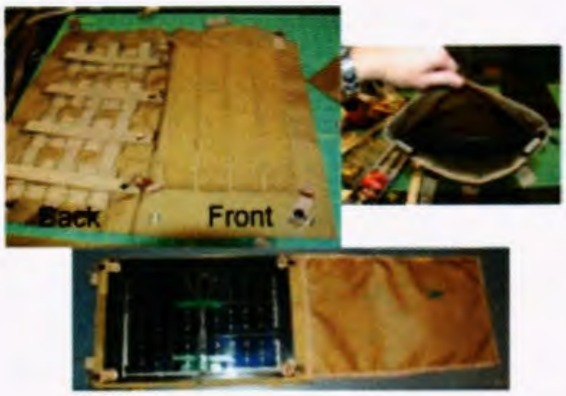

Fig. 13. MSP carrier.

TABLE I
ENERGY HARVESTED BY THE MSP CONTROL PANELS THROUGHOUT THE LOE-1

Date	Flat Panel	Tracking Panel	Comments
2/6/2012	35.6 Whrs	47.4 Whrs	Partly sunny
2/7/2012	44.9 Whrs	98.0 Whrs	Sunny
2/8/2012	10.8 Whrs	11.0 Whrs	Cloudy/Rain
2/9/2012	46.3 Whrs	100.3 Whrs	Sunny
Cumulative	137.6 Whrs	256.7 Whrs	

The remaining three MSP systems were used as controls by NRL to establish a baseline for the field test. The control measurements consisted of total solar insolation, solar panel output in various deployment configurations, and battery charging capability. The three control panels were set up in a variety of four different configurations throughout the week: tracking the sun while charging a battery, lying horizontally flat while charging a battery, lying horizontally flat while collecting *I–V* data, and tracking while collecting *I–V* data. All of these configurations helped to understand how the system worked as a whole, as well as the maximum amount of charge that the BB-2590s could have received throughout the experiment.

B. LOE-1 Experimental Results

1) Control Group Results: The LOE-1 experiment provided a very good environment to test the MSP systems, as the weather was both sunny and cloudy over the four days. The MSP solar panel performance measured in both the flat and tracking configurations over the test days is summarized in Table I. The flat panels produced ~138 Wh over the four days, while the tracking panels produced ~257 Wh. This can be compared with the total capacity of the BB-2590, which is 175 Wh. The typical daily energy need of a dismounted Marine is between 25 and 125 Wh and is based on radio type and usage. The data show the clear advantage of solar tracking versus a stationary, flat panel. The data also show reasonable energy harvesting even during a cloudy day, which is an important result as it demonstrates good performance of the MSP panels in low-light conditions. This is further investigated in Fig. 14, where the panel output is plotted as a function of illumination intensity. The MSP panel efficiency is seen to be constant with illumination intensity.

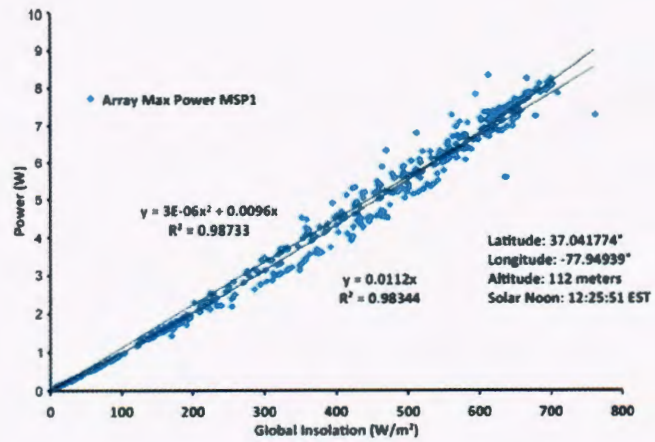

Fig. 14. Power output of an MSP panel measured as a function of solar insolation. These data demonstrate that the MSP panels function well independent of the illumination intensity.

TABLE II
BATTERY CHARGING DATA FROM MSP CONTROL GROUP

Date	Orientation	Sun Energy	Array Power	Battery Power	Array Efficiency	Charging Efficiency	Est System Efficiency
		Whrs	Whrs	Whrs	%	%	%
2/6/12	FLAT	194.2	33	4.86	17.0	14.7	2.5
2/6/12	TRACKED	215.6	47.4	36.34	22.0	76.7	16.9
2/7/12	FLAT	236.2	44.9	19.80	19.0	44.1	8.4
2/8/12	FLAT	60.7	11.5	5.74	18.9	49.9	9.5
2/8/12	FLAT	60.7	11.5	2.59	18.9	22.5	4.3
2/9/12	FLAT	244.5	46.3	19.90	18.9	43.0	8.1
2/9/12	FLAT	244.5	46.3	17.96	18.9	38.8	7.3

The next step in the analysis is to determine how much of the solar energy harvested by the MSP panels was transferred to the batteries. A summary of the battery charging achieved by the control group systems is given in Table II. These data show that while the solar panels displayed good efficiency, the battery charging efficiency was extremely low; therefore, the overall system efficiency was low. It was concluded that the poor charging efficiency was due to a nonoptimized design of the power box, and can be fixed easily.

2) Group 1 and 2 Results: The results show between 0.6 and 12.6 Wh delivered to a battery over two days and 2.6–32.2 Wh over four days. This data are of only limited use; however, because of the poor performance of the power control circuit. Furthermore, the solar panels showed some integrity problems including interconnect stresses and bypass diode shorting, which affected the data that gathered from the LOE-1. The Marine carried MSP system does not include a solar insolation measurement; therefore, there is significant uncertainty in the actual system efficiency due to no recorded data of the solar insolation each panel experienced.

VI. COMPARISON OF MOBILE SOLAR POWER WITH CURRENT SYSTEMS

While there are other flexible PV technologies currently being developed [6], [7], MSP is most comparable with the current USMC Program of Record (POR) PV powered battery charging system: the Solar Portable Alternative Communications Energy System (SPACES). The SPACES solar panel consists of copper

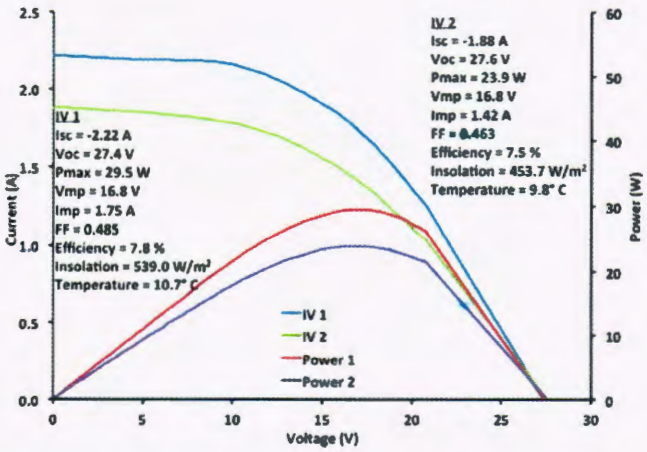

Fig. 15. Outdoor measurements of CIGS panel from a SPACES unit made as part of a side-by-side comparison with an MSP panel.

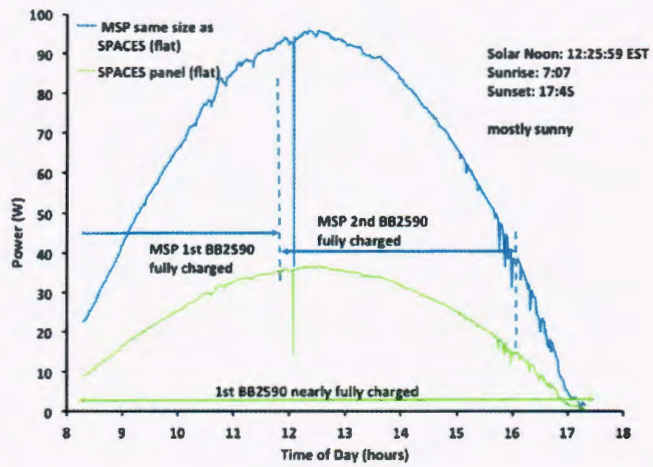

Fig. 16. Modeled performance of an MSP and SPACES panel based on the measured performance given in Figs. 5 and 15, where the panel power output has been calculated throughout the day.

TABLE III
SIDE-BY-SIDE MEASUREMENT OF MSP AND SPACES

Panel	Panel Efficiency (%) (Cell Active Area)	Panel Efficiency (%) (Total Panel Area)
MSP	19.6	11.60
SPACES	7.8	5.58

indium gallium diselenide (CIGS) solar cells mounted in a panel that can be folded. NRL performed a side-by-side, outdoor test of an MSP and a SPACES panel. The panels were laid flat (horizontal orientation) during the test. The cell active area of the MSP panel is 0.06 m^2 and that of the SPACES panel is 0.7 m^2. The MSP total panel was 0.26 m by 0.39 m (0.101 m^2). The SPACES panel was 1.321 m by 0.746 m (0.985 m^2). The measured data are shown in Fig. 15. The results are summarized in Table III. The MSP panel efficiency of 19.6% (active cell area calculation) compares well with the measured individual solar cell efficiency of ~22% (see Fig. 2).

These results indicate that the MSP panel produces approximately twice the power than the SPACES blanket. To show the operational implications of this, the power output of an MSP panel as a function of time throughout one day at Fort Pickett in VA (February 9, 2012) was calculated and compared with similar data for a SPACES blanket. In this modeling effort, the MSP panel was assumed to be the same size as the SPACES panel, 0.985 m^2, with the same packing density as for the existing MSP panels. The solar insolation was determined from the SMARTS model, as described earlier. The results are shown in Fig. 16. The MSP panel produces 2.6× the power of the SPACES blanket, which means that, during this day in February in VA, the MSP panel can recharge two BB-2590 batteries, whereas the SPACES panel can barely charge one.

VII. SUMMARY AND FUTURE PLANS

The results of the MSP deployment during the LOE-1 demonstrated excellent performance of the solar panels, showing more than a factor of two improvement over the current POR (SPACES). It can be concluded that the MSP solar panel technology is an enabling technology for portable power. The results for charging a BB-2590 were less positive, as the best system charging efficiency attained was approximately 17%.

The next step in the MSP program is to improve the solar cell interconnect issues and produce several more panels that demonstrate improved ruggedness. The panels will also be designed to allow them to be connected in parallel so Marines can charge a single battery more quickly when stationary.

The battery charge control issue will be addressed by coordinating the MSP project with the Squad Electric Power Network (SEPN). SEPN is an ONR Future Naval Capability (FNC) project with the goal of creating a Marine worn power network system connecting energy generation sources with batteries and an array of loads such as radios and night vision goggles. SEPN is currently developing a charge control unit capable of taking input from a solar panel and using that input to charge a BB-2590 as well as power the electrical loads. The MSP panel appears to be a natural fit for this, and the redesigned MSP panels will be used during the LOE-2.2 in July 2012 to test the functionality of SEPN and MSP.

The present results have demonstrated the performance of the mobile solar technology; therefore, efforts must now be placed on making the technology rugged and affordable.

REFERENCES

[1] R. Tatavarti, G. Hillier, A. Dzankovic, G. Martin, F. Tuminello, R. Navaratnarajah, G. Du, D. P. Vu, and N. Pan, "Lightweight, low cost GaAs solar cells on 4″ epitaxial liftoff (ELO) wafers," in *Proc. 33rd IEEE Photovoltaic Specialists Conf.*, May 2008, pp. 1–4.

[2] R. Tatavarti, A. Wibowo, G. Martin, F. Tuminello, C. Youtsey, G. Hillier, N. Pan, M. W. Wanlass, and M. Romero, "InGaP/GaAs/InGaAs inverted metamorphic (IMM) solar cells on 4″ epitaxial lifted off (ELO) wafers," in *Proc. 35th IEEE Photovoltaic Spec. Conf.*, Jun. 2010, pp. 002125–002128.

[3] C. Gueymard, Simple Model of the Atmospheric Radiative Transfer of Sunshine (SMARTS), ver. 2.9.5, 2009

[4] [Online]. http://www.bren-tronics.com/bt-70791a.html, last access Feb. 2, 2012.

[5] [Online]. http://en.wikipedia.org/wiki/MOLLE, last access Feb. 2, 2012.

[6] Y. Kishi, H. Inoue, H. Tanaka, S. Kouzuma, K. Murata, S. Sakai, M. Nishikuni, K. Wakisaka, H. Shibuya, H. Nishiwaki, A. Takeoka, and Y. Kuwano, "New type of ultralight flexible a-Si solar cell and its application on an airplane," in *Proc. 22nd IEEE Photovoltaic Spec. Conf.*, Oct. 1991, pp. 1213–1218.

[7] J. Park, H. Ham, J. Lee, and T. Kim, "Thin film encapsulation for flexible organic solar cells," in *Proc. 35th IEEE Photovoltaic Spec. Conf.*, Jun. 2010, pp. 001657–001659.

Kelly M. Trautz was born in Hackensack, NJ, on November 1, 1986. She received the Bachelor of Science in engineering science degree, with a specialization in mechanical engineering, from Loyola University Maryland, Baltimore, in May 2008, and the Master of Engineering Management degree from the University of Maryland, Baltimore, in May, 2011.

She has been working as a Mechanical Engineer for the U.S. Naval Research Laboratory, Washington, DC, since 2008. She has been a member of Project Management Institute (PMI) since 2009 and has served as a volunteer in the position of Educational Director of Finance for the organization since February 2012. Her current research interests include renewable energy and photovoltaic systems.

Phillip P. Jenkins, photograph and biography not available at the time of publication.

Robert J. Walters, photograph and biography not available at the time of publication.

David Scheiman, photograph and biography not available at the time of publication.

Raymond Hoheisel, photograph and biography not available at the time of publication.

Rao Tatavarti, photograph and biography not available at the time of publication.

Ray Chan, photograph and biography not available at the time of publication.

Haruki Miyamoto, photograph and biography not available at the time of publication.

Jessica G. J. Adams, photograph and biography not available at the time of publication.

Victor C. Elarde, photograph and biography not available at the time of publication.

James Grimsley, photograph and biography not available at the time of publication.

AIP Applied Physics Letters

W-structured type-II superlattice long-wave infrared photodiodes with high quantum efficiency

E. H. Aifer, J. G. Tischler, J. H. Warner, I. Vurgaftman, W. W. Bewley et al.

Citation: Appl. Phys. Lett. **89**, 053519 (2006); doi: 10.1063/1.2335509
View online: http://dx.doi.org/10.1063/1.2335509
View Table of Contents: http://apl.aip.org/resource/1/APPLAB/v89/i5
Published by the American Institute of Physics.

Additional information on Appl. Phys. Lett.
Journal Homepage: http://apl.aip.org/
Journal Information: http://apl.aip.org/about/about_the_journal
Top downloads: http://apl.aip.org/features/most_downloaded
Information for Authors: http://apl.aip.org/authors

ADVERTISEMENT

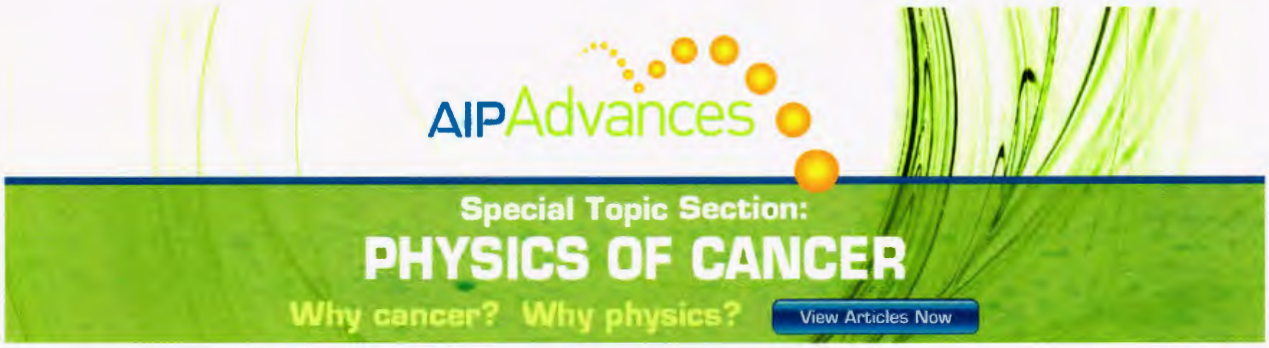

Downloaded 10 Jul 2012 to 132.250.22.5. Redistribution subject to AIP license or copyright; see http://apl.aip.org/about/rights_and_permissions

W-structured type-II superlattice long-wave infrared photodiodes with high quantum efficiency

E. H. Aifer,[a] J. G. Tischler, J. H. Warner, I. Vurgaftman, W. W. Bewley, J. R. Meyer, J. C. Kim, and L. J. Whitman
Naval Research Laboratory, Washington, DC 20375

C. L. Canedy and E. M. Jackson
SFA Inc., Crofton, Maryland 21114

(Received 18 April 2006; accepted 21 June 2006; published online 4 August 2006)

Results are presented for an enhanced type-II W-structured superlattice (WSL) photodiode with an 11.3 μm cutoff and 34% external quantum efficiency (at 8.6 μm) operating at 80 K. The new WSL design employs quaternary $Al_{0.4}Ga_{0.49}In_{0.11}Sb$ barrier layers to improve collection efficiency by increasing minority-carrier mobility. By fitting the quantum efficiencies of a series of *p-i-n* WSL photodiodes with background-doped *i*-region thicknesses varying from 1 to 4 μm, the authors determine that the minority-carrier electron diffusion length is 3.5 μm. The structures were grown on semitransparent *n*-GaSb substrates that contributed a 35%–55% gain in quantum efficiency from multiple internal reflections. © *2006 American Institute of Physics*. [DOI: 10.1063/1.2335509]

W-structured type-II superlattices (WSLs), which were initially developed to increase the gain in midwave infrared (MWIR) lasers,[1,2] are now showing promise as long-wave and very-long-wave infrared (LWIR and VLWIR) photodiode materials. The WSL addresses the reduced overlap between the wave functions for conduction and valence states in type-II superlattices, arising from the alternating electron and hole confinement layers. In the WSL illustrated in Fig. 1, two InAs "electron wells" are located on either side of an InGaSb hole well and are bound on either side by AlSb (dashed) or AlGaInSb (solid) "barrier" layers. The barriers confine the electron wave functions symmetrically about the hole well, increasing the electron-hole overlap while nearly localizing the wave functions. The resulting quasi-two-dimensional densities of states give the WSL its characteristically strong absorption near the band edge. Care is taken to not fully localize the wave functions, however, since an electron miniband is required to allow vertical transport of the photoexcited minority carriers.

The use of WSLs in photodiodes was first reported by Fuchs *et al.*,[3] who investigated structures designed for MWIR laser operation. Mixed results were obtained relative to photodiodes employing binary and ternary type-II superlattices (BSLs and TSLs), with the WSLs exhibiting good transport characteristics, but quantum efficiency (QE) hampered by large series resistance. We have more recently resumed the investigation of WSL photodiodes, extending operation to the LWIR and VLWIR bands.[4] Initial designs adapted from WSL lasers yielded transport results comparable to those for BSL and TSL photodiodes, but significantly lower QEs. Since transmission measurements confirmed strong absorption, this was attributed to poor collection of the photoexcited carriers. It also raised concerns that WSLs, with their longer period, additional interfaces, high Al content, and reduced electron mobility, might necessarily have low QE.

In this letter we describe a second generation of WSL-based LWIR photodiodes, in which improvements to the design and material quality have strongly reduced minority-carrier losses and substantially improved the QE. By measuring QE in a series of WSL *p-i-n* photodiodes grown with identical heterostructures but with varying background-doped *i*-region (BD-region) thickness, we are able to extract the minority-carrier diffusion length.

Figure 1 specifies the thickness and composition of each layer employed in the four-constituent periodic WSL structure, which was designed for a nominal band gap of 11.3 μm. Here the AlSb barriers of the earlier WSL photodiodes are replaced by quaternary barrier layers (QBLs), consisting of $Al_{0.4}Ga_{0.49}In_{0.11}Sb$. Since the QBL contains 60% less Al, its optimal growth temperature is much closer to that of the InAs and InGaSb layers. The QBL conduction band offset with respect to InAs is also substantially reduced, from 2.1 eV for AlSb barriers to 1.3 eV for the QBL. This results in a near doubling of the electron miniband width, from 20 to 35 meV, and therefore an enhancement of the vertical electron mobility.

Five WSL *p-i-n* photodiodes were grown with BD regions having thicknesses of 1, 1.5, 2, 3, and 4 μm, in a Riber compact 21 T solid-source molecular beam epitaxy (MBE)

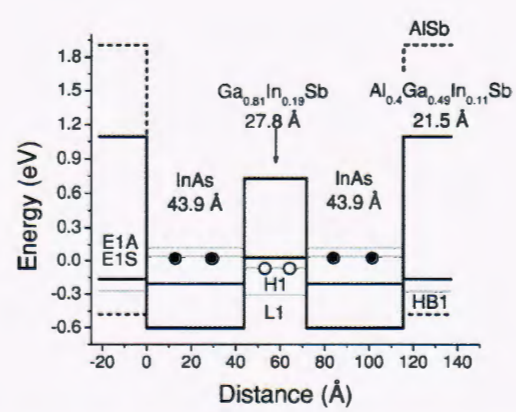

FIG. 1. Band profiles and energy levels at $k=0$ of enhanced WSL with quaternary barrier layers. Dashed lines indicate the position AlSb bands for comparison.

[a]Electronic mail: aifer@estd.nrl.navy.mil

 © 2006 American Institute of Physics

Downloaded 10 Jul 2012 to 132.250.22.5. Redistribution subject to AIP license or copyright; see http://apl.aip.org/about/rights_and_permissions

system. Each *p-i-n* structure was grown on a *n*-type (Te doped 1×10^{17} cm^{-3}) GaSb substrate, beginning with a thick p^+-GaSb contact layer doped with Be to $(1-3)\times10^{18}$ cm^{-3}, followed by a 0.1-μm-thick *p*-WSL that was Be doped to 4×10^{17} cm^{-3}. The BD region was grown next, followed by 0.33 μm of n^+-WSL, Si doped to 4×10^{17} cm^{-3}. The structures were capped with a 10-nm-thick n^+-InAs contact layer, Si doped to 4×10^{17} cm^{-3}.

The target structure was designed to be strain compensated with neutral interfaces. This was motivated by an earlier study[5] that linked strong degradation of the photoluminescence (PL) intensity with the use of group III soaks to force InSb-like interface bonds. Even without group III soaks, however, cross-sectional scanning tunneling microscopy has revealed that MBE background levels and segregation can still induce the predominance of a particular bond type, and hence strain.[6] WSL test structures were therefore grown and evaluated for strain and periodicity by x-ray diffraction and for band gap and overall material quality by PL measurements. To the extent that background As levels and Sb segregation could be eliminated, the nominally lattice matched WSL alloy recipe was typically adjusted in the final calibration growth to minimize strain. While this procedure produced wafers with negligible strain (120 ppm maximum, <50 ppm typical) and uniformly high PL intensity, superlattice period was allowed to vary by as much as 5% (2 ML), resulting in a cutoff wavelength range from 9.3 to 11.3 μm. This was acceptable for the purposes of this study since peak QE is fairly insensitive to band gap.

Unpassivated, circular mesa diodes with 100–400 μm diameters were isolated by wet etching to a depth of 1.5–4.5 μm to the p^+-GaSb contact layer. Ti/Pt/Au Ohmic contacts were then deposited on both the n^+-InAs top and exposed p^+-GaSb bottom contact layers. The contacts were windowed or were small relative to the mesa size to provide optical access to the top-illuminated photodiodes.

The external QE was determined from the photocurrent excited in the sample by a calibrated blackbody operating at 1000 K and at a distance of 10.9 in. The blackbody flux, chopped at 37 Hz, was incident through a narrow bandpass filter, centered at 5.34 μm with a 0.35 μm full width at half maximum. To reduce stray reflections, the sample was enclosed in a cold shield with a half-angle field of view of $\approx10°$. The average QE within the filter passband was then used to rescale the normalized QE spectrum obtained with a Fourier transform infrared spectrometer. Independent QE measurements on several samples were also performed at Rockwell Scientific Co. and Northwestern University.

In Fig. 2, typical QE spectra for each *p-i-n* photodiode are plotted for comparison. The QE is seen to increase systematically with absorber thickness, with the external QE (measured at 8.6 μm and averaged over 20 photodiodes) reaching a value of 34% for the 4-μm-thick device, which had a 50% power responsivity cutoff wavelength of 11.3 μm. This is among the highest reported for an antimonide type-II superlattice photodiode.[7,8] The *I-V* characteristics yielded average dynamic-impedance-area products (R_0A) of 10–20 Ω cm^2 at 80 K, also comparable to the best type-II values,[9] although still about a factor of 10 lower than the state of the art for HgCdTe photodiodes in this wavelength range. Surface resistivities of $\approx(1-2)\times10^4$ Ω cm along the unpassivated sidewalls were obtained from the inverses of the slopes of $(R_0A)^{-1}$ versus mesa perimeter-to-area

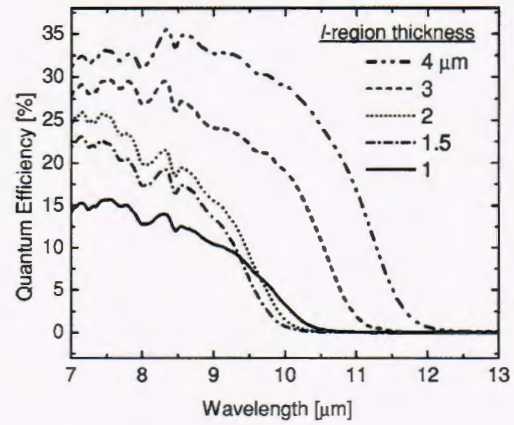

FIG. 2. Quantum efficiency spectra of WSL photodiodes with 1–4-μm-thick background-doped *i*-regions. Each spectrum is representative of the average for the sample.

ratio. These relatively high values of surface resistivity indicate suppressed rates of band-to-band and trap-assisted tunneling, which are prevalent where the high field region of the junction is exposed. We believe that the suppression of tunneling current in WSLs is due mainly to the very large electron effective mass along the growth axis, relative to that of binary and ternary type-II superlattices.

In a *p-i-n* photodiode, the quantum efficiency is largely determined by three factors: the absorption coefficient, the background impurity concentration in the BD region (N_{bgnd}), and the minority-carrier diffusion length (L_n). While the absorption coefficient determines the rate of optical generation, N_{bgnd} and L_n determine the volume over which photoexcited carriers can contribute significant photocurrent, through drift or diffusion processes, respectively. In an ideal *p-i-n* diode, the background impurity concentration is negligible and the built-in electric field extends across the entire *i* region and sweeps all photoexcited carriers across the junction. If the residual doping levels are appreciable, however, the field is restricted to a relatively short depletion region and most photoexcited carriers must diffuse a significant distance across the quasineutral *i* region to be collected. In this case, the minority-carrier diffusion length is a critical factor determining the detector quantum efficiency.

This behavior can be quantified using Hovel's expression[10] for the external QE of a *p-n* junction, with the surface recombination velocity set equal to zero. The total QE is expressed as sum over three regions,

$$\mathrm{QE} = \mathrm{QE}_{p\text{-}n} + \mathrm{QE}_{\mathrm{SCR}} + \mathrm{QE}_{n\text{-}p}. \tag{1}$$

The contribution from the space charge region (SCR) is

$$\mathrm{QE}_{\mathrm{SCR}} = (1-R)(e^{-\alpha x_n} - e^{-\alpha x_p}), \tag{2}$$

where QE depends only on the reflectivity of the top surface R, on the absorption coefficient α, and on N_{bgnd} through the boundaries of the *n* and *p* depletion regions x_n and x_p. The collection of minority electrons from the quasineutral *p* region ($\mathrm{QE}_{n\text{-}p}$), however, is a strong function of the electron diffusion length L_n and its ratio with the width of this region W_H,

Downloaded 10 Jul 2012 to 132.250.22.5. Redistribution subject to AIP license or copyright; see http://apl.aip.org/about/rights_and_permissions

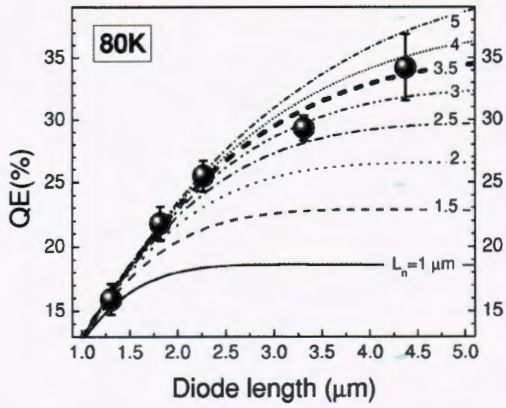

FIG. 3. Scatter plot of peak QE of WSL photodiodes vs length, from the beginning of the n region to the end of p-background-doped region. Lines are plots of Hovel's expression [Eqs. (1)–(3)], with the electron diffusion length as a fitting parameter.

$$\mathrm{QE}_{n\text{-}p} = (1-R)\frac{\alpha L_n}{(\alpha L_n)^2 - 1} e^{-\alpha x_p}\left[\alpha L_n - \frac{\sinh(W_H/L_n) + \alpha L_n e^{-\alpha W_H}}{\cosh(W_H/L_n)}\right]. \quad (3)$$

A similar contribution from the quasineutral n region, $\mathrm{QE}_{p\text{-}n}$, is minimal because that layer is thin and heavily doped and has a low minority-carrier hole mobility.

The background doping of the i region was determined from measurements on a Hall sample, consisting of a 2-μm-thick undoped WSL grown over a 1-μm-thick lattice matched $AlAs_{0.4}Sb_{0.92}$ layer to isolate the WSL from the conductive n-GaSb substrate. A quantitative mobility spectrum analysis[11] of the magnetic-field-dependent (0–9 T) Hall data determined electron and hole carrier densities and mobilities versus temperature. The results show a p-type background concentration of $\approx 2\times 10^{15}\ \mathrm{cm}^{-3}$ with a mobility of $\approx 5000\ \mathrm{cm}^2/\mathrm{V\,s}$ at 80 K.

One remaining issue is that the line shapes exhibited in Fig. 2 are atypical of the WSL spectra expected from the absorption measurements, since they lack the characteristic peak near cutoff, and also exhibit sharp, oscillatory features having a fixed pattern. These features correspond to the transmission spectrum of the metal-filled epoxy used to bond the samples to the gold plated chip carriers. Transmission measurements show that the 500-μm-thick n-GaSb substrates (Te doped $1\times 10^{17}\ \mathrm{cm}^{-3}$) transmit nearly 85% of the incident light not reflected at the interface (at 7.5 μm). It is therefore evident that multiple internal reflections contribute significantly to the measured QE. Based on QE measurements of a p-i-n photodiode using the same heterostructure with a 2-μm-thick BD region grown on an absorbing p-GaSb substrate, we estimate that the measured QE is enhanced by 35% for the 4-μm-thick BD-region sample to 55% for the sample with the 1-μm-thick absorber. The corresponding single-pass QE values are then 10%, 14.6%, 17.5%, 20%, and 25% for the 1-, 1.5-, 2-, 3-, and 4-μm-thick absorber layer samples, respectively. This effect results in a further underestimation of the diffusion length, since the relative increase in QE due to reflections increases as the strongly absorbing BD-region thickness decreases.

In Fig. 3, solid circles are used to plot the measured QE peak nearest cutoff as a function of diode length including the n-doped and BD regions. Simulations using Hovel's expression (lines), with the electron diffusion length as a fitting parameter, are plotted for comparison. The best fit is obtained for an electron diffusion length of $L_n \approx 3.5\ \mu$m and an absorption coefficient of 2200 cm^{-1} at 7.5 μm, which represents a lower bound on L_n since we set the surface recombination velocity to zero. While transmission measurements on the photodiode wafers yielded a value of 1600 cm^{-1} for the absorption coefficient, the value used for fitting is enhanced by 40% owing to multiple reflections in packaged devices as discussed above. Finally, almost no enhancement in photoresponse under reverse bias was observed in photodiodes with active regions less than 4 μm thick, in further confirmation that the diffusion length was in excess of 3 μm.

Our results demonstrate that despite the WSL's additional complexity, including twice as many interfaces per period and reduced electron mobility along the growth axis, WSL photodiodes can achieve high QE relative to other type-II superlattice systems.

The authors gratefully acknowledge Manijeh Razeghi and Andrew Hood at Northwestern University and Gernot Hildebrandt at Rockwell Scientific Co. for providing independent QE measurements of several of the samples in this letter. This work was supported by the Office of Naval Research and the Missile Defense Agency.

[1] J. R. Meyer, C. A. Hoffman, F. J. Bartoli, and L. R. Ram-Mohan, Appl. Phys. Lett. **67**, 757 (1995).
[2] C. L. Canedy, W. W. Bewley, J. R. Lindle, I. Vurgaftman, C. S. Kim, M. Kim, and J. R. Meyer, Appl. Phys. Lett. **86**, 211105 (2005).
[3] F. Fuchs, L. Burkle, R. Hamid, N. Herres, W. Pletschen, R. E. Sah, R. Kiefer, and J. Schmitz, Proc. SPIE **4288**, 171 (2001).
[4] E. H. Aifer, J. G. Tischler, J. H. Warner, I. Vurgaftman, J. C. Kim, J. R. Meyer, B. R. Bennett, L. W. Whitman, E. M. Jackson, and J. R. Lorentzen, Proc. SPIE **5732**, 259 (2005).
[5] C. L. Canedy, W. W. Bewley, C. S. Kim, M. Kim, I. Vurgaftman, and J. R. Meyer, J. Appl. Phys. **94**, 1347 (2003).
[6] E. M. Jackson, G. Boishin, E. H. Aifer, B. R. Bennett, and L. W. Whitman, J. Cryst. Growth **270**, 301 (2004).
[7] Y. Wei, A. Gin, and M. Razeghi, Appl. Phys. Lett. **80**, 3262 (2002).
[8] Y. Wei, A. Hood, V. Yazdanpanah, M. Razeghi, M. Z. Tidrow, and V. Nathan, Appl. Phys. Lett. **86**, 091109 (2005).
[9] R. Rehm, M. Walther, F. Fuchs, J. Schmitz, and J. Fleissner, Appl. Phys. Lett. **86**, 173501 (2005).
[10] H. J. Hovel, *Semiconductors and Semimetals* (Academic, New York, 1975), Vol. 11, pp. 17–20.
[11] I. Vurgaftman, J. R. Meyer, C. A. Hoffman, D. Redfern, J. Antoszewski, and L. Faraone, J. Appl. Phys. **84**, 4966 (1998).

Downloaded 10 Jul 2012 to 132.250.22.5. Redistribution subject to AIP license or copyright; see http://apl.aip.org/about/rights_and_permissions

AIP Applied Physics Letters

Double quantum-well tunnel junctions with high peak tunnel currents and low absorption for InP multi-junction solar cells

Matthew P. Lumb, Michael K. Yakes, María González, Igor Vurgaftman, Christopher G. Bailey et al.

Citation: Appl. Phys. Lett. **100**, 213907 (2012); doi: 10.1063/1.4722890
View online: http://dx.doi.org/10.1063/1.4722890
View Table of Contents: http://apl.aip.org/resource/1/APPLAB/v100/i21
Published by the American Institute of Physics.

Related Articles

Non-linear luminescent coupling in series-connected multijunction solar cells
Appl. Phys. Lett. 100, 251106 (2012)

Enhanced performance by incorporation of zinc oxide nanowire array for organic-inorganic hybrid solar cells
Appl. Phys. Lett. 100, 243102 (2012)

Amorphous/crystalline silicon heterojunction solar cells via remote inductively coupled plasma processing
Appl. Phys. Lett. 100, 233902 (2012)

Direct and charge transfer state mediated photogeneration in polymer–fullerene bulk heterojunction solar cells
Appl. Phys. Lett. 100, 193302 (2012)

Direct and charge transfer state mediated photogeneration in polymer–fullerene bulk heterojunction solar cells
APL: Org. Electron. Photonics 5, 106 (2012)

Additional information on Appl. Phys. Lett.

Journal Homepage: http://apl.aip.org/
Journal Information: http://apl.aip.org/about/about_the_journal
Top downloads: http://apl.aip.org/features/most_downloaded
Information for Authors: http://apl.aip.org/authors

ADVERTISEMENT

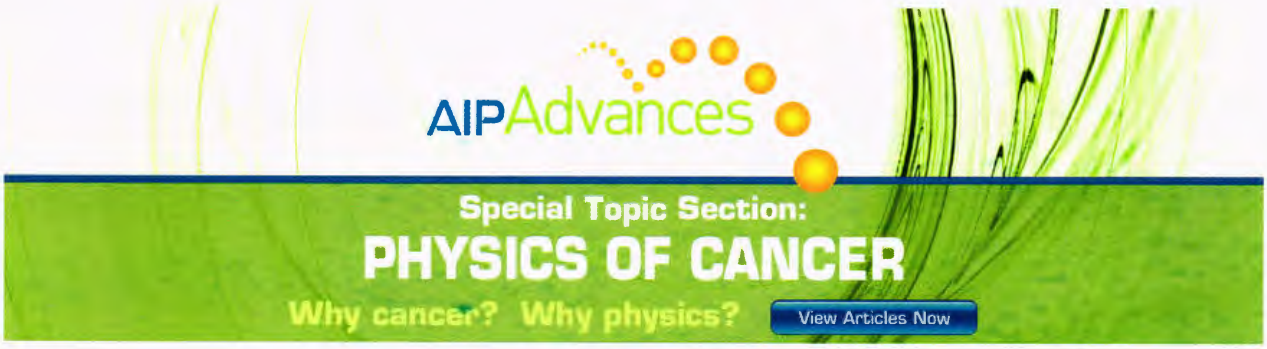

Downloaded 05 Jul 2012 to 132.250.22.5. Redistribution subject to AIP license or copyright; see http://apl.aip.org/about/rights_and_permissions

Double quantum-well tunnel junctions with high peak tunnel currents and low absorption for InP multi-junction solar cells

Matthew P. Lumb,[1,2] Michael K. Yakes,[2] María González,[2,3] Igor Vurgaftman,[2] Christopher G. Bailey,[2] Raymond Hoheisel,[1,2] and Robert J. Walters[2]
[1]*The George Washington University, 2121 I Street NW, Washington DC 20037, USA*
[2]*Naval Research Laboratory, Washington DC 20375, USA*
[3]*Sotera Defense Solutions, 2200 Defense Highway, Suite 405, Crofton, Maryland 21114, USA*

(Received 30 March 2012; accepted 11 May 2012; published online 24 May 2012)

Lattice matched InAlGaAs tunnel junctions with a 1.18 eV bandgap have been grown for a triple-junction solar cell on InP. By including two InGaAs quantum wells in the structure, a peak tunnel current density of 113 A/cm^2 was observed, 45 times greater than the baseline bulk InAlGaAs tunnel junction. The differential resistance of the quantum well device is 7.52×10^{-4} Ω cm^2, a 15-fold improvement over the baseline device. The transmission loss to the bottom cell is estimated to be approximately 1.7% and a network simulation demonstrates that quantum well tunnel junctions play a key role in improving performance at high sun-concentrations. © *2012 American Institute of Physics*. [http://dx.doi.org/10.1063/1.4722890]

Tunnel junctions (TJs), or Esaki diodes,[1] are an important component of multi-junction solar cells, connecting the subcells of a monolithic multi-junction stack in electrical series. For optimal performance, it is important that the TJ has a high enough peak tunnel current density not to impede the flow of photocurrent between the subcells, which can reach tens of A/cm^2 in sun-concentrator applications.[2] Also, the differential resistance of the tunnel diode should be as low as possible to minimize any voltage drop across the diode. A final consideration for solar cell applications is that the TJ should be as transparent as possible to light below the band gap of the cell directly above the TJ, both to minimize the filtering of the light to the cell beneath and also to minimize the possibility of photocurrent being produced by the TJ.[3–5]

In this work, we discuss the development of a tunnel junction designed to operate between the middle and bottom cells of an InP-based triple junction (3J) solar cell. InP-based multi-junction cells are a promising route to high conversion efficiencies in both terrestrial and extra-terrestrial environments, and there have been recent successes in developing component cells for the InP-based 3J.[6] The optimum bandgap configurations for the 3J under different spectra were determined by Gonzalez *et al.*[7] The middle cell bandgap derived from this work was chosen to be 1.18 eV, achieved using the lattice-matched quaternary $In_{0.52}Al_{0.33}Ga_{0.15}As$. A basic p^{++}/n^{++} tunnel junction was produced using this material and compared to an identical structure containing a pair of lattice-matched $In_{0.53}Ga_{0.47}As$ quantum wells, providing much more efficient interband tunneling. Similar structures grown by other authors have been shown to exhibit very high tunnel currents and peak to valley ratios (PVR) in the past.[8,9] In this work, however, we examine the trade-off in the improved tunneling characteristics and the increased transmission loss using the quantum wells compared to the bulk TJ. Using a combination of IV characterization and modeling, the relative performance of the quantum well TJ and the bulk TJ was measured, with the quantum well tunnel junction (QWTJ) demonstrating a greater than 45-fold increase in the peak tunnel current and a greater than 15-fold reduction in the differential resistance, with only a small impact on the transparency.

To evaluate the performance of the QWTJ versus a baseline device, two test structures were fabricated, one of which contained the QWTJ structure and the other contained the conventional bulk TJ structure. The device structures are summarized in Figure 1. The structures were grown using solid source molecular beam epitaxy. Each tunnel junction is surrounded by a 1500 Å 2×10^{17} cm^{-3} Si-doped (n-type) $In_{0.53}Ga_{0.47}As$ buffer layer beneath and a 1500 Å

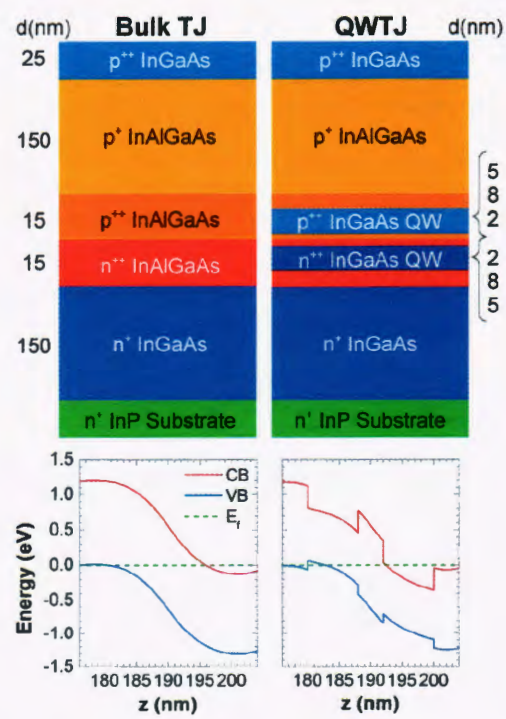

FIG. 1. A schematic diagram of the baseline bulk InAlGaAs TJ structure (left) and the QWTJ structure, incorporating two 80 Å InGaAs QWs (right). Calculated equilibrium band diagrams for the junction region of the two structures are shown (bottom).

 © 2012 American Institute of Physics

Downloaded 05 Jul 2012 to 132.250.22.5. Redistribution subject to AIP license or copyright; see http://apl.aip.org/about/rights_and_permissions

$2 \times 10^{17}\,cm^{-3}$ Be-doped (p-type) $In_{0.52}Al_{0.33}Ga_{0.15}As$ buffer layer above. These buffer layers were chosen to resemble the base and emitter regions of InAlGaAs and InGaAs middle and bottom cells in a 3J architecture. A 250 Å $1 \times 10^{19}\,cm^{-3}$ Si-doped $In_{0.53}Ga_{0.47}As$ cap layer was used to achieve an Ohmic contact to the front surface, and all the structures were grown on n-type InP wafers. The baseline bulk TJ has 150 Å $In_{0.52}Al_{0.33}Ga_{0.15}As$ $1 \times 10^{19}\,cm^{-3}$ Si-doped and $1 \times 10^{19}\,cm^{-3}$ Be-doped layers. The QWTJ device has two 80 Å QWs separated by a 40 Å $In_{0.52}Al_{0.33}Ga_{0.15}As$ barrier and with 50 Å $In_{0.52}Al_{0.33}Ga_{0.15}As$ barriers either side, and the QWTJ device is designed so that the total thickness and doping are identical to the bulk TJ. The wafers were processed into circular devices with a mesa diameter of 1 mm and the current voltage characteristics were measured using a four point probe technique.

The equilibrium band structure of the devices was calculated using semiconductor band-solver software developed at the Naval Research Laboratory. The software numerically solves Poisson's equation in one dimension for a given layer structure, using band parameters taken from Vurgaftman *et al.*[10] The band diagrams for the bulk TJ and QWTJ are shown in Figure 1. The QWTJ calculation assumed the bulk properties of InGaAs within the quantum wells which provide a good first approximation to the band structure of the QWTJ. However, quantum confinement effects modify the density of states in the QW regions and, strictly speaking, need to be accounted for, which will be the subject of further study.

The electrical characteristics of representative diodes of the bulk TJ and QWTJ are shown in Figure 2. The bulk TJ demonstrated a clear negative differential resistance (NDR) region, with a peak tunnel current density of 2.52 A/cm^2 and a peak to valley ratio of 4.8. Assuming a typical triple junction 1-sun short circuit current density of 15 mA/cm^2, the peak tunnel current density corresponds to a concentration ratio (CR) of approximately 170 suns. The differential resistance of the tunnel diode was found to be $1.15 \times 10^{-2}\,\Omega\,cm^2$. In comparison, the QWTJ demonstrated a much higher peak tunnel current density of 112.9 A/cm^2, a factor of approximately 45 greater than the bulk TJ. In order to see the NDR in the two devices clearly, the IV curves are presented in Figure 2 on semi-log axes. The equivalent concentration of this current is approximately 7500 suns, which far exceeds the requirements for terrestrial concentration applications. A small differential resistance is extremely important for minimizing voltage losses in multi-junction solar cells, and the QWTJ exhibited a differential resistance of $7.52 \times 10^{-4}\,\Omega\,cm^2$, which is a factor of 15.3 lower than the bulk diode. The PVR of the QWTJ was 10.7, and it is believed that this figure can be improved through further optimization of the barrier and well thicknesses.

The proposed mechanism for improving the tunneling characteristics of the diode is the efficient tunneling via the confined electron and hole energy levels of the quantum wells.[9] Using bulk materials of a narrower bandgap, such as lattice-matched InGaAs, is well known to improve the resonant interband tunneling probability[5] and high peak tunnel currents have been demonstrated using InGaAs TJs.[11] However, the benefit of the InGaAs QWs with wider bandgap barriers compared to a bulk InGaAs TJ is that efficient tunneling can be achieved with a much smaller impact on the transparency of the diode. It is important that the TJ is transparent to light lower in energy than the $In_{0.52}Al_{0.33}Ga_{0.15}As$ middle cell bandgap to minimize the filtering of light to the bottom cell. To approximate the absorption in the double QWTJ compared to bulk InGaAs beyond the middle cell bandgap, the absorption coefficient was calculated using the analytical solution to the finite square well problem in the effective mass approximation and in the absence of an electric field. This gives a rough estimate of the absorption coefficient and energy level structure of each well, although in reality the electric field across the wells significantly modifies the envelope wavefunctions and confined energies.[12] The confined energy levels of the quantum wells are displayed in the inset to Figure 3. The density of states was calculated using the familiar two dimensional density of states expression and the absorption coefficient then calculated using the overlap integrals deduced from the solution of the finite QW problem and the interband momentum matrix elements. For simplicity, the Coulombic attraction of the

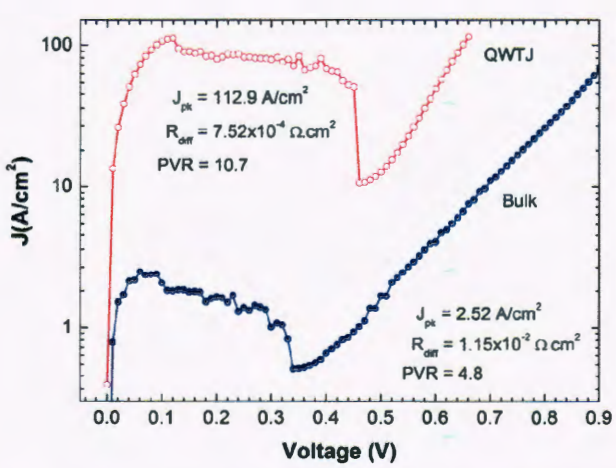

FIG. 2. A semi-log plot of current density versus voltage for the bulk TJ and the QWTJ measured using a four-point-probe technique.

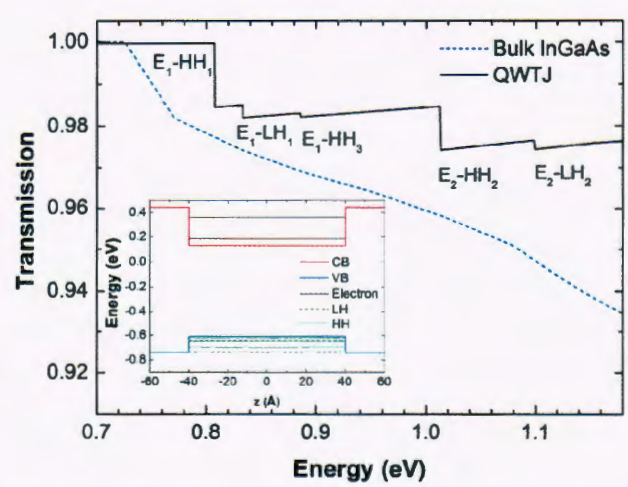

FIG. 3. The calculated transmission of the double QW region of the QWTJ compared to the same thickness of bulk InGaAs. The inset shows the confined energy levels in the InGaAs quantum well.

Downloaded 05 Jul 2012 to 132.250.22.5. Redistribution subject to AIP license or copyright; see http://apl.aip.org/about/rights_and_permissions

electrons and holes and broadening mechanisms were neglected. A more detailed description of the absorption calculation can be found in, for example, Ref. 13. The absorption calculated in this way can be seen as an upper limit, as the significant electric field across the QW region reduces the overlap integral of the electron and hole wavefunctions, thereby weakening the absorption. Therefore, the actual transmission losses during operation in the solar cell may be smaller than the estimate from this simple QW model.

The transmission of light below the InAlGaAs bandgap is shown in Figure 3 for both the QWTJ and bulk InGaAs. In the QWTJ case, the transmission was calculated using a transfer matrix technique, which takes into account the multiple reflections at the well/barrier interfaces, although the low index contrast of the layers results in a very small effect. The layer structure was two 80 Å QWs separated by a 40 Å InAlGaAs barrier and surrounded by two 50 Å InAlGaAs barriers, as shown in Figure 1. The substrate and ambient layers were assumed to be InAlGaAs also, to avoid the complications of multiple reflections at the front and rear surfaces of the structure. The real part of the refractive index for the QW layers was assumed to be that of bulk InGaAs. The transmission is compared to the single pass transmission through 300 Å of bulk InGaAs calculated using the Beer-Lambert law.

Results show that the transmission through the QWTJ is attenuated by approximately 1% per well above the lowest energy confined state of the well, and as shown in Figure 3 the transmission in the QWTJ is significantly greater than a bulk InGaAs TJ of the same overall thickness. This is important when considering the use of these structures within the 3J device. The power density contained in the ASTM AM1.5 g spectrum between the energies of 0.74–1.18 eV is 165.8 W/m^2, and for the baseline InAlGaAs TJ it is assumed that all this power is transmitted through the junction region of the TJ. In the case of bulk InGaAs, 3.9% of the available light in this spectral region is absorbed. However, with the QWTJ only 1.7% of the light in this spectral band is absorbed. Even though the effect is reduced, the absorption in the QWs does still create a loss mechanism for the 3J solar cell. However, as discussed earlier, this simple QW model gives an upper limit to the transmission losses which may be lower in a real device. Furthermore, by using InAlGaAs QWs with a wider bandgap, it may be possible to lower the trade off in peak tunnel current and absorption.

To evaluate the trade-off in the transparency and differential resistance of the bulk and QWTJ structures, we used a network simulation of an idealized 3J solar cell with bandgaps of 1.74 eV, 1.18 eV, and 0.74 eV. A similar approach to Steiner *et al.*[14] was employed and a schematic layout of the network simulation is shown in the inset to Figure 4. The simulation was split into nine illuminated components and one shaded component, each with an area of 1×10^{-6} cm^2, forming a cross-section between a grid finger and the halfway point of two grid fingers. Any voltage drop along the direction of the grid finger was neglected, allowing the network to extend only in one direction. The saturation current of the subcells was estimated from the radiative recombination limit[7] and values of 7.5×10^{-27} A/cm^2, 8.9×10^{-18} A/cm^2, and 8.9×10^{-11} A/cm^2 were used for the top, middle, and bottom cells, respectively, assuming a temperature of 300 K.

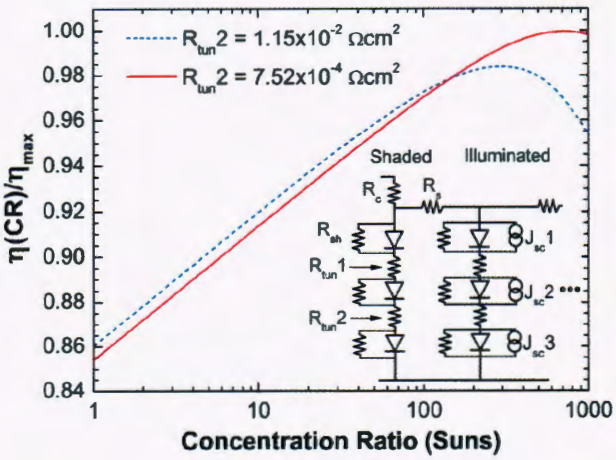

FIG. 4. Calculated values of normalized efficiency as a function of the CR for idealized 3 J devices using the bulk (dotted blue line) and QW (solid red line) tunnel junctions. The inset shows a schematic of the network simulation layout.

The solar cell with the bulk TJ was chosen to be perfectly current matched and the short circuit current density for each sub-cell was arbitrarily chosen to be 15 mA/cm^2 under one sun conditions. We assumed that there was a linear relationship between the J_{sc} of the subcells and the solar CR. Each cell had a shunt resistance of 1×10^8 Ω cm^2, the spreading resistance of the top of the cell was assumed to be 200 $\Omega/\square$ and the contact resistance used a value of 3×10^{-6} Ω cm^2. The tunnel diodes were represented as resistors with the measured values of differential resistance from the bulk and QWTJ structures. This method allows a direct comparison of the differential resistance on the solar cell efficiency, but obviously does not take in to account the non-linearity of the tunnel diode. The differential resistance of the TJ between the first and second sub-cells was fixed at 1×10^{-4} Ω cm^2. To account for the absorption loss with the QWTJ, the short circuit current of bottom cell was reduced by 1.7%, making the 3J overall bottom cell limited.

Figure 4 shows the simulated efficiency of the 3J cells normalized to the peak efficiency. At low concentrations, the filtering of the light to the bottom cell reduces the conversion efficiency of the 3J with the QWTJ by approximately 0.7% relative to the baseline TJ, due to the bottom cell limiting the current. However, for concentrations above 140 suns the QWTJ device becomes more efficient due to the lower resistive loss, and at 1000 suns the QWTJ device has approximately a 4.4% higher efficiency relative to the bulk device. In reality, once the concentration ratio exceeds approximately 170 suns, the increase in efficiency of the QWTJ will be greater still due to the photocurrent exceeding the peak tunnel current of the bulk TJ. This will cause the bulk TJ to pass current in the thermal diffusion mode, thereby incurring a much larger voltage drop.[14] The small absorption loss in the QWTJ device therefore has only a very small impact on the performance at high concentration due to the much smaller resistive loss.

In conclusion, we have demonstrated a quantum well tunnel junction structure which can be used to improve the performance of a multi-junction solar cell. By incorporating two InGaAs QWs, a peak tunnel current of 113 A/cm^2 was

Downloaded 05 Jul 2012 to 132.250.22.5. Redistribution subject to AIP license or copyright; see http://apl.aip.org/about/rights_and_permissions

observed, which was a 45-fold increase over the baseline InAlGaAs TJ, and a differential resistance of $7.52 \times 10^{-4}\ \Omega\ \mathrm{cm}^2$, which was a 15.3-fold improvement over the baseline device. The increase in the spectral power absorbed in the QW region is estimated to be about 1.7%, which is significantly smaller than a bulk InGaAs TJ which absorbs 3.9%. This yields a device which can far surpass the electrical performance of the conventional tunnel junction structure at high concentrations with minimal transmission loss. We believe that the design can be further optimized to improve the transparency whilst still achieving extremely high peak tunnel currents by tailoring the QW depth and the barrier thickness. In addition to the role in developing multi-junction solar cells on InP, analogous QWTJs could improve the performance of the more established 3J devices based on Ge or GaAs substrates.

The author would like to thank Woojun Yoon, Chaffra Affouda, and Joe Tischler for valuable contributions to this work. This work was supported by the Office of Naval Research.

[1]L. Esaki, Phys. Rev. **109**(2), 603 (1958).
[2]F. Dimroth, Phys. Status Solidi C **3**, 373 (2006).
[3]M. Yamaguchi, Sol. Energy Mater. Sol. Cells **75**(1–2), 261 (2003).
[4]M. Yamaguchi, K.-I. Nishimura, T. Sasaki, H. Suzuki, K. Arafune, N. Kojima, Y. Ohsita, Y. Okada, A. Yamamoto, T. Takamoto, and K. Araki, Sol. Energy **82**(2), 173 (2008).
[5]J. F. Wheeldon, C. E. Valdivia, A. W. Walker, G. Kolhatkar, A. Jaouad, A. Turala, B. Riel, D. Masson, N. Puetz, S. Fafard, R. Arès, V. Aimez, T. J. Hall, and K. Hinzer, Prog. Photovoltaics **19**(4), 442 (2011).
[6]M. S. Leite, R. L. Woo, W. D. Hong, D. C. Law, and H. A. Atwater, Appl. Phys. Lett. **98**(9), 093502 (2011).
[7]M. González, N. Chan, N. J. Ekins-Daukes, J. G. J. Adams, P. Stavrinou, I. Vurgaftman, J. R. Meyer, J. Abell, R. J. Walters, C. D. Cress, and P. P. Jenkins, in *Proceedings of SPIE, Physics and Simulation of Optoelectronic Devices XIX*, San Francisco, edited by B. Witzigmann, F. Henneberger, Y. Arakawa, and A. Freundlich (SPIE, 2011).
[8]S. Sutar, Q. Zhang, and A. Seabaugh, IEEE Trans. Electron Devices **57**(10), 2587 (2010).
[9]H. H. Tsai, Y. K. Su, H. H. Lin, R. L. Wang, and T. L. Lee, IEEE Electron Device Lett. **15**(9), 357 (1994).
[10]I. Vurgaftman, J. R. Meyer, and L. R. Ram-Mohan, J. Appl. Phys. **89**(11), 5815 (2001).
[11]G. M. Cohen, D. Ritter, and C. Cytermann, Electron. Lett. **31**(17), 1511 (1995).
[12]D. A. B. Miller, D. S. Chemla, T. C. Damen, A. C. Gossard, W. Wiegmann, T. H. Wood, and C. A. Burrus, Phys. Rev. B. **32**(2), 1043 (1985).
[13]J. Singh, *Electronic and Optoelectronic Properties of Semiconductor Structures* (Cambridge University Press, Cambridge, 2003).
[14]M. Steiner, W. Guter, G. Peharz, S. P. Philipps, F. Dimroth, and A. W. Bett, Prog. Photovoltaics **20**(3), 274 (2011).

Downloaded 05 Jul 2012 to 132.250.22.5. Redistribution subject to AIP license or copyright; see http://apl.aip.org/about/rights_and_permissions

Invited Paper

Quantum wells and superlattices for III-V photovoltaics and photodetectors

Matthew P. Lumb*[a,b], Igor Vurgaftman[b], Chaffra A. Affouda[b], Jerry R. Meyer[b], Edward H. Aifer[b] and Robert J. Walters[b]
[a]The George Washington University, 2121 I Street NW, Washington DC, 20037, USA
[b]US Naval Research Laboratory, Washington DC, 20375, USA

ABSTRACT

Semiconductor quantum wells and superlattices have found numerous applications in optoelectronic devices, such as lasers, LEDs and SOAs, and are an increasingly common feature of high efficiency solar cells and photodetectors. In this paper we will highlight some of the recent developments in the use of low-dimensional III-V semiconductors to improve the performance of photovoltaics by tailoring the bandgap of the junction. We also discuss novel structures designed to maximize photo-generated carrier escape and the application of quantum confinement to other components of the solar cell, such as tunnel junctions. Recent developments in type-II superlattices for photodetectors will also be discussed, including the graded-gap LWIR device based on the W-structured superlattices demonstrated at the Naval Research Laboratory. Modeled results will be presented using the NRL BANDS™ integrated 8-band k·p and Poisson solver, which was developed for computing the bandstructures of superlattice and multi-quantum well photodiodes.

1. INTRODUCTION

Low-dimensional semiconductors play an important role in the operation of a range of optical and electronic devices, and are widely studied by researchers investigating semiconductor theory and experiment, crystal growth and material science. Advances in epitaxial growth techniques have led to the realization of sophisticated quantum heterostructures, able to exploit the quantum nature of electrons and holes when confined on length scales comparable to the de Broglie wavelength of the carriers. Two important examples of low-dimensional semiconductors are quantum wells (QWs) and superlattices (SLs) that use one dimensional confinement to tailor the electronic properties of the material. QWs and SLs are an established technology for a range of devices including lasers, light emitting diodes and semiconductor optical amplifiers. In this work we highlight two specific applications of QWs and SLs, for photovoltaic solar cells and photodetectors, in which quantum confinement for bandgap engineering can improve the device performance and flexibility.

2. QUANTUM WELL SOLAR CELLS

The incorporation of quantum wells into the intrinsic region of a solar cell to extend the absorption range was first proposed by Keith Barnham [1] at Imperial College London. By controlling the thickness and composition of the QWs, the absorption edge of the solar cell can be tuned to optimize the cell performance under the terrestrial solar spectrum. The problems associated with growing well materials with lattice mismatch to the host substrate can be mitigated by choosing the barrier material and thickness to compensate the strain introduced by the QW - a technique known as strain balancing [2]. This approach allows multiple quantum well (MQW) stacks with >100 periods to be grown without introducing strain related defects or dislocations [3, 4].

The motivation for tailoring the bandgap of a solar cell can be well understood by performing detailed balance calculations of the cell's limiting efficiency. In the detailed balance limit, the dark current of the solar cell is limited only by radiative recombination and the external quantum efficiency (EQE) is assumed to be 100%. The calculated limiting efficiency then guides the search for optimal bandgap, or configuration of bandgaps in a multi-junction cell, that most efficiently converts a given spectrum into electrical power. To represent an MQW stack in the detailed balance model we use an approach similar

Next Generation (Nano) Photonic and Cell Technologies for Solar Energy Conversion III,
edited by Loucas Tsakalakos, Proc. of SPIE Vol. 8471, 84710A · © 2012 SPIE
CCC code: 0277-786/12/$18 · doi: 10.1117/12.964654

Downloaded From: http://proceedings.spiedigitallibrary.org/ on 04/01/2013 Terms of Use: http://spiedl.org/terms

to that outlined by Adams *et al.*[5]. The bulk regions of the solar cell, in this case GaAs, have unity external quantum efficiency, whereas the extended absorption of the MQW region has a variable quantum efficiency and bandgap value, as shown in figure 1. The dark current is calculated using the Generalized Planck expression in the Boltzmann limit [6], using the EQE values defined in the model. The photocurrent is calculated using the EQE integrated with the ASTM AM1.5G spectrum.

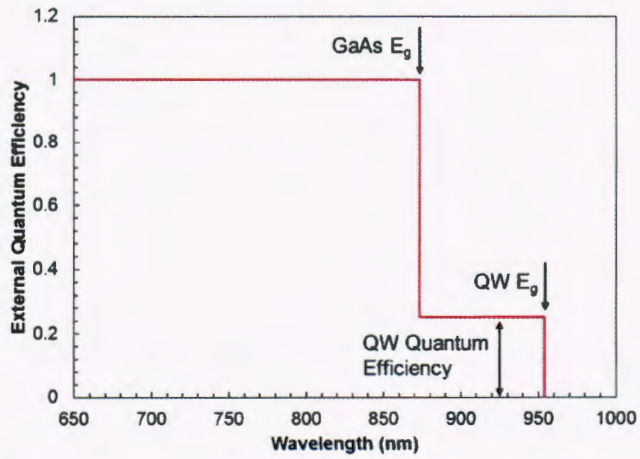

Figure 1. The idealized quantum efficiency of a QW solar cell, with variable QW bandedge and external quantum efficiency.

The conversion efficiency of a single junction GaAs solar cell incorporating an MQW stack is shown in figure 2a. The thick red line indicates the iso-efficiency contour for the GaAs solar cell. For strongly absorbing MQW stacks with EQE approaching unity, modest efficiency enhancements are found for QW bandgaps smaller than the GaAs value, up to a maximum improvement of approximately 0.5% absolute for an MQW stack with 1.34eV bandgap. If the MQW quantum efficiency is low, however, the conversion efficiency can be lower than the baseline GaAs material if the extra photocurrent produced by the MQW does not outweigh the increase in dark current from the narrow gap MQW region. Nonetheless, using MQWs as part of a multi-junction architecture has clear advantages [7].

A fundamental limitation of the well-established triple junction (3J) based on Germanium for concentrator and space applications is that the bandgap of the $In_{0.01}Ga_{0.99}As$ middle cell is wider than is optimal for a 3J cell with a Ge bottom cell. Figure 2b shows the conversion efficiency of the Ge-based 3J if the middle cell contains MQWs and the bottom and top cell bandgaps are fixed at 0.67eV and 1.85eV, respectively. Whereas the conversion efficiency for the bulk 3J is calculated to be 40.4%, it is improved significantly when QWs with relatively modest quantum efficiencies are included. This is because the extra photocurrent improves the current matching of the top two cells, far outweighing the voltage reduction induced by including the wells. While the actual gains expected from inclusion of the QWs are somewhat smaller since the top cell can be thinned to reduce the current mismatch in the top and middle cells, commercially available 3J MQW cells containing 70 QWs with 1.32eV bandgap gave a 3% absolute increase in efficiency over a comparable, current-matched, bulk baseline device [8].

Downloaded From: http://proceedings.spiedigitallibrary.org/ on 04/01/2013 Terms of Use: http://spiedl.org/terms

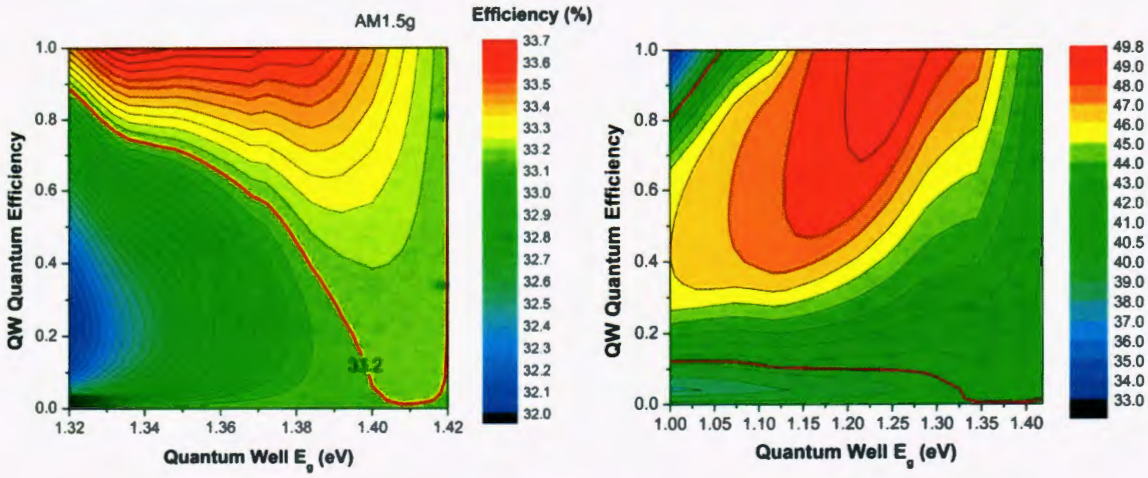

Figure 2. (a) The limiting efficiency of a single junction QWSC with variable QW bandgap and external quantum efficiency. (b) The limiting efficiency of a triple junction solar cell incorporating a QWSC as the middle cell. The top and bottom cell bandgaps are fixed at 1.85 and 0.67 eV, respectively.

A further consideration for terrestrial PV is the spectral variability due to location, the angle of the sun and varying atmospheric conditions. Although cell performance under the standard reference spectrum is a good benchmark indicator for competing technologies, the total energy harvested at a given actual location provides a preferable measure of cell performance. Using reliable, time resolved atmospheric data and the SMARTS2 model [9], realistic spectra were generated for a variety of locations and combined with a detailed model for quantum well solar cells by Lumb *et al.* [10]. Even when the top cell base thicknesses of both the bulk and MQW 3J devices were tailored to maximize the energy harvest, the MQW cell outperformed the bulk device. The advantage is particularly noticeable in locations where the spectral content is red-rich for large parts of the year, such as Solar Village in Saudi Arabia. By capitalizing on its longer absorption edge that exploits the increased light content at longer wavelengths, the MQW cell gave gains of approximately 3% over a year of simulated operation.

3. NOVEL STRUCTURES FOR MAXIMIZING CARRIER ESCAPE

Recent work at the University of Tokyo [11] and University of Houston [12] has focused on enhancing carrier escape from the quantum wells through resonant tunneling. In a highly-confined quantum well system, the thermionic escape time for photogenerated carriers is predicted to be long due to the large potential barrier. A potential route to shortening this time is to provide a local tunneling escape path by including a thin well in close proximity to the thicker absorbing well. Carriers photogenerated in the thicker well can efficiently tunnel to the neighboring well, thereby creating a sequential thermionic and tunneling escape mechanism with a shorter lifetime than for purely thermionic escape. This concept is shown schematically for the conduction band of a coupled QW system in figure 3. The red arrow shows the thermionic escape path from the lowest energy state in the quantum well whereas the black lines show a combined tunneling and thermionic escape mechanism. This technology may prove particularly valuable for systems requiring very deep QWs to substantially lengthen the absorption edge.

Downloaded From: http://proceedings.spiedigitallibrary.org/ on 04/01/2013 Terms of Use: http://spiedl.org/terms

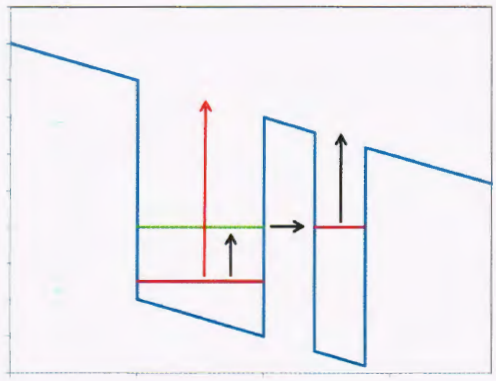

Figure 3. Schematic diagram showing two different escape mechanisms from a QW system. The red arrow shows thermionic escape directly from the thicker well, whereas the black arrows show a combined thermionic and tunneling escape mechanism.

4. QUANTUM WELL TUNNEL JUNCTIONS

In addition to using quantum wells for bandgap engineering, recent work at the Naval Research Laboratory has demonstrated that QWs can also enhance the performance of tunnel junctions [13]. Tunnel junctions are an important component of multi-junction solar cells that require a low differential resistance to minimize voltage losses, as well as a large peak tunneling current density to facilitate the flow of photocurrents as large as tens of A/cm^2 in high solar concentration situations [14]. Tunnel junctions to interconnect the middle and bottom cells of an InP-based triple junction cell were designed and grown using Molecular Beam Epitaxy (MBE). The baseline device was an $In_{0.52}Al_{0.33}Ga_{0.15}As$ tunnel diode with 150 Å p^{++}/n^{++} layers. The tunneling region was surrounded by a 1500Å $In_{0.52}Al_{0.33}Ga_{0.15}As$ layer above and a 1500 Å $In_{0.53}Ga_{0.47}As$ buffer layer beneath, which are similar to the base and emitter of the surrounding cells in a full multi-junction architecture. In the quantum well tunnel junction (QWTJ), the total thickness and doping were identical to those of the baseline device, except that two 80 Å, lattice matched $In_{0.53}Ga_{0.47}As$ quantum wells were included in the p^{++} and n^{++} regions respectively. The QWs were separated by a 40Å barrier. Figure 4 shows secondary-ion mass spectroscopy (SIMS) measurements of the Si and Be dopant concentrations in the baseline and QWTJ structures.

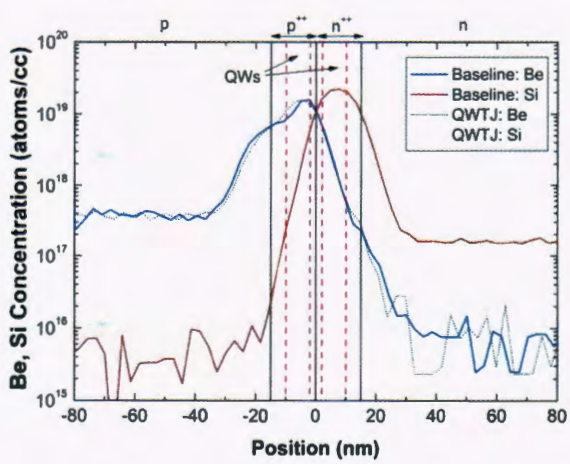

Figure 4. SIMS measurements showing the Be and Si dopant concentrations in the QWTJ and baseline bulk samples. The doping profiles in the two structures are seen to be nominally identical.

Downloaded From: http://proceedings.spiedigitallibrary.org/ on 04/01/2013 Terms of Use: http://spiedl.org/terms

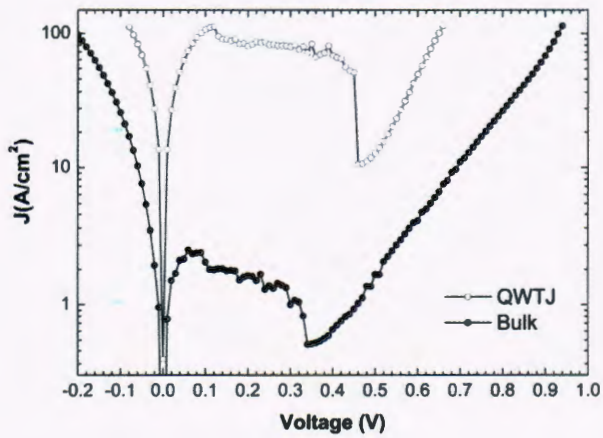

Figure 5. Measured current-voltage characteristics for the QWTJ (open points) and baseline bulk (closed points) devices. The peak tunnel current for the QWTJ is seen to be greater by a factor of 45.

The QWTJ device exhibited a peak tunnel current density of 113 A/cm^2, which was 45 times greater than the baseline bulk InAlGaAs tunnel junction. The QW device's differential resistance of 7.52×10^4 Ωcm^2, was a 15-fold improvement over the baseline device. The current-voltage characteristics of the baseline bulk device and the QWTJ are shown in figure 5, on semi-log axes for clarity. The QWs absorb a small fraction of the light beyond the InAlGaAs middle cell absorption edge, resulting in up to 1.7% transmission loss to the bottom cell for light in the 0.74-1.18eV spectral range according to a simple QW absorption coefficient model [13]. However, for high-concentration applications, reduced differential resistance is expected to outweigh the slightly higher optical loss.

5. MODELING SUPERLATTICES USING A K·P APPROACH

In order to design optimal quantum confined structures for solar cells and photodetectors, appropriate analytical tools are needed to realistically model the bandstructures of periodic multilayered media. This section describes the NRL BANDS™ software package that we developed to calculate quantum well and superlattice bandstructures within the k·p approximation. The theoretical framework is similar to that outlined by Vinter *et al.* [15] with all the band parameters taken from the review article of Vurgaftman *et al.* [16]. The effects of biaxial strain on the relevant band parameters is included, under the assumption that the layers are grown pseudomorphically on to the host substrate. The k·p model provides an efficient method for calculating the SL band structure near to the zone boundary, which is used to extract the band properties needed to create an effective medium for the superlattice. When used in conjunction with a numerical solution of Poisson's equation, this effective medium provides a computationally inexpensive method for calculating the equilibrium band diagrams of SL devices.

In order to calculate the SL eigenstates, we represent them as a z-dependent expansion of the Bloch waves in the material. The coefficients of the expansion are further expanded in a Fourier series over the spatial frequency of the superlattice. The eigenstates of the SL are represented by z-dependent envelope-function approximations:

$$\varphi_{nk}(r) = \sum_{m,i} a_n^{m,i}(k) e^{jG_m z} e^{jk.r} u_{i0}(r;z) \tag{1}$$

The envelope functions are expanded in a Fourier series over discrete spatial frequencies of the superlattice $G_m=2\pi m/d$, where d is the SL period, m indexes the number of Fourier components retained and u_{i0} is the periodic Bloch function at k=0 for orbital i. We use 8 orbitals: S, P_X, P_Y, P_Z including spin degeneracy. The eigenvalue problem for the periodic superlattice is then given by

Downloaded From: http://proceedings.spiedigitallibrary.org/ on 04/01/2013 Terms of Use: http://spiedl.org/terms

$$H_{SL}\varphi_{nk} = E_n(k)\varphi_{nk} \tag{2}$$

Here H_{SL} is an $8*N \times 8*N$ matrix, where N is the number of Fourier components and $E_n(k)$ is the energy dispersion for band n. This k·p approach is valid up to approximately 10-20% of the Brillouin zone. From the calculated energy band dispersion the effective medium properties are derived, including the bandgap, relative valence band energy level, and in-plane and out-of-plane effective masses for electrons and holes. The bandgap of the effective medium is defined as the energy separation of the electron and hole ground-state energies at k=0. The SL mini-bands are evaluated at k_z=0 and the edge of the SL Brillouin zone, $k_z=\pi/d$. The mini-band width calculated in the z direction at $k_{\|}$=0 is given by

$$W_n = E_n\left(k_z = \frac{\pi}{d}\right) - E_n(k_z = 0) \tag{3}$$

A Cosine function provides a good approximation for the dispersion in the z direction

$$E_n(k_z) = \frac{W_n}{2}(1 - \cos k_z d) - E_n(0) \tag{3}$$

The effective mass in the z direction is therefore given by

$$m_{z,n} = \frac{2\hbar^2}{W_n d^2} \tag{4}$$

The in-plane mass for each band is calculated from the in-plane curvature of the band at k=0. The lattice constant and static permittivity are averaged from the bulk material parameters, weighted by the layer thicknesses. Conduction and valence band effective medium masses are calculated by averaging, using Boltzmann weighting over the first few bands

$$m_{avg} = \frac{\sum_i m_i \exp\left(-\frac{E_i - E_1}{k_B T}\right)}{\sum_i \exp\left(-\frac{E_i - E_1}{k_B T}\right)} \tag{5}$$

This ensures that the curvature of the lowest lying energy bands dominate the carrier effective mass. If $|W_n| \gg k_B T$ for the lowest energy electron or hole band, the overall medium effective mass is a three dimensional average, with a value given by the geometric mean of the averaged in-plane and out of plane masses

$$m_{3D}^* = \left(m_{avg,z} m_{avg,\|}{}^2\right)^{1/3} \tag{6}$$

On the other hand, if $|W_n| < k_B T$ for the lowest-energy electron or hole subband, that subband is assumed to be effectively two dimensional and therefore only the in-plane mass is considered

Downloaded From: http://proceedings.spiedigitallibrary.org/ on 04/01/2013 Terms of Use: http://spiedl.org/terms

$$m^*_{2D} = m_{avg,\parallel} \tag{7}$$

The default use of 2D or 3D effective masses can be overwritten at runtime. Figure 6 shows the growth axis (left) and in-plane (right) dispersion relations derived by NRL BANDS™ for two electron and four hole subbands in a representative simple type-II InAs/$In_{0.1}Ga_{0.9}Sb$ SL, grown on GaSb. Note that the lowest energy electron subband is 3D in nature, while the ground-state hole subband is 2D. The calculated in-plane effective masses for electrons and holes subbands are $0.024m_0$ and $0.035m_0$, respectively.

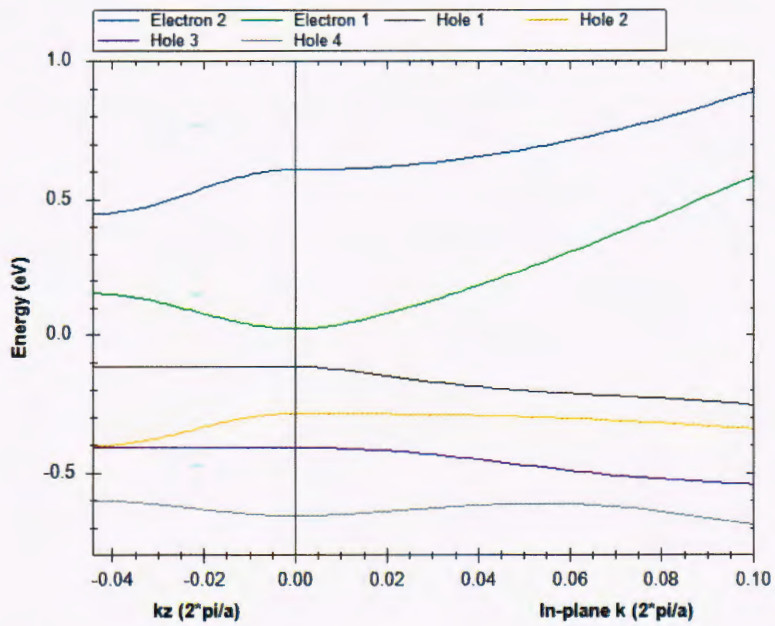

Figure 6. Calculated growth-axis (left panel) and in-plane (right panel) energy dispersion of the two lowest electron and four lowest hole subbands in a simple SL consisting of 40.9Å InAs layers alternating with 27.6Å $In_{0.1}Ga_{0.9}Sb$ layers at 77 K. The structure is strain-compensated for growth on a GaSb substrate.

Figure 7 shows the equilibrium band diagram at 77K of an n-i-p heterojunction [17], whose LWIR absorber layer is a type-II InAs/InGaSb SL. The *n*-type side of the heterojunction is a second type-II superlattice whose periodic layering of 47.0Å InAs layer and 20.4Å $Al_{0.89}In_{0.11}Sb$ provides a much wider bandgap of 0.46eV at 77K. The full structure consists of a 300nm 4×10^{17} cm^{-3} *n*-type InAs/AlInSb SL, a 300nm intrinsic InAs/AlInSb SL (1×10^{15} cm^{-3} *n*-type background doping is assumed), a 1000 nm 1×10^{16} cm^{-3} *p*-type InAs/GaInSb absorber SL, and a 500nm 1×10^{18} cm^{-3} *p*-type GaSb buffer layer. The software is designed to provide a simple and intuitive visualization of the band diagram, carrier concentrations, electrostatic potential, doping profiles, and band alignments for complicated heterostructure architectures. The software automatically defines a simulation mesh to give an efficient yet accurate solution of Poisson's equation, although the mesh can be modified by the user at runtime. In addition, the user is able to overwrite the default band parameters, so that fine adjustments can be made to fit the experimental data.

Downloaded From: http://proceedings.spiedigitallibrary.org/ on 04/01/2013 Terms of Use: http://spiedl.org/terms

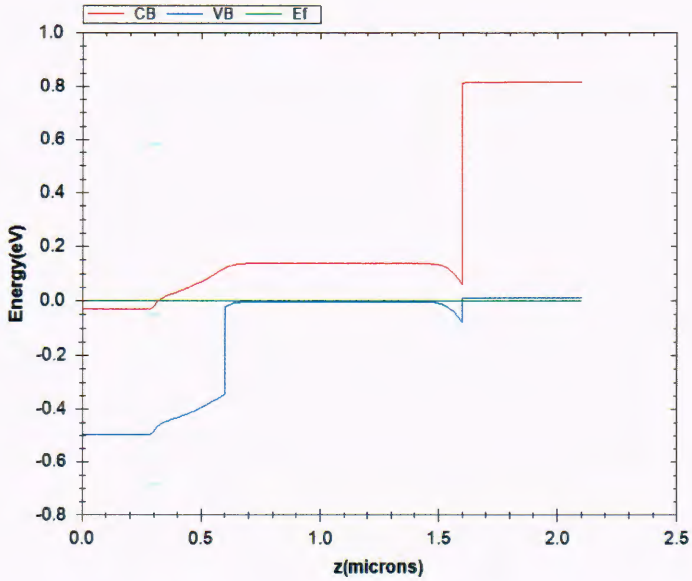

Figure 7. Equilibrium band diagram of an *nip* heterojunction SL structure grown on a GaSb buffer layer, calculated at 77K.

6. W-STRUCTURE SL AND GRADED BANDGAP LWIR PHOTODETECTORS

A four layer periodic superlattice developed at the Naval Research Laboratory, known as the W-structure due to the conduction band offset profile, has enabled the realization of type-II MWIR lasers with higher gain as well as LWIR detector materials with enhanced absorption turn-on near the bandedge. Table 1 shows a single period of an example W-structure superlattice (WSL) for the detector absorber region, grown on GaSb, from Canedy *et al.* [18].

Table 1. The layer structure of a single period of a WSL absorber region, grown on GaSb.

Material	Thickness Å
InAs	18
$Ga_{0.7}In_{0.3}Sb$	34
InAs	18
$AlAs_{0.106}Sb_{0.894}$	234

Figure 8 shows the output for the ground state conduction and valence band profiles, energy levels and wavefunction probability distributions of the lowest electron and hole subbands in arbitrary units. The highest valence subband is found to have a heavy hole character. Because of its additional degrees of freedom, the four-layer W-structure can readily provide a graded band gap with independently tunable conduction and valence offsets, while also maintaining strain compensation and fixed GaInSb alloy composition for practical growth by MBE. This approach was used by Vurgaftman *et al.* [19] to grow a graded bandgap type-II LWIR photodetector that displayed significantly suppressed tunneling and generation-recombination dark currents at low temperature, with comparable dark current performance to state of the art HgCdTe devices. Recent improvements in device fabrication using shallow etch mesa isolation (SEMI) has enabled a significant reduction in excess dark current through sidewall leakage and bulk junction currents in graded gap structures [20]. A shallow etch, terminating only 10-20nm past the junction, defines individual photodiodes while leaving the narrow-gap absorber layer buried 100 nm to 200 nm below the surface. This allows separate optimization of the photodiode's electrical and optical area. The bulk junction current can be lowered by reducing the junction area to a fraction of the pixel dimension, without lowering the quantum efficiency of the photodiode. Using this technique, high-quality imaging focal-plane-arrays using the graded bandgap W-structure concept have been fabricated [17].

Downloaded From: http://proceedings.spiedigitallibrary.org/ on 04/01/2013 Terms of Use: http://spiedl.org/terms

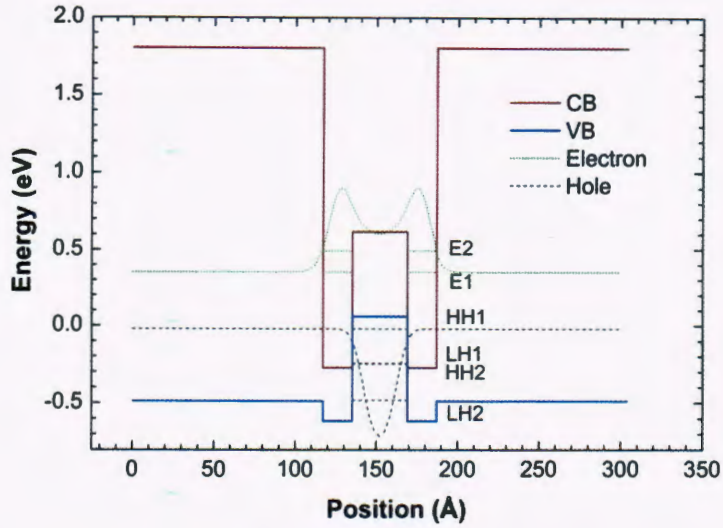

Figure 8. Conduction and valence band profiles, subband energies for the lowest two electron and four hole sub-bands, and wavefunction probability distributions for the electron and hole ground states in a type II LWIR W-structure superlattice at 300K.

7. CONCLUSION

In this paper we have outlined several examples where the incorporation of quantum-confined multilayers is beneficial to the operation of photovoltaics and photodetectors. Bandgap-engineered, multi-quantum well photovoltaic devices have shown enhanced performance over bulk counterparts, and have the potential to improve the energy harvest efficiencies in real world solar concentrator applications. We have discussed the latest research on long wavelength quantum well photovoltaics with efficient carrier extraction geometries, and discussed the role of quantum wells in high performance tunnel diodes that serve as subcell interconnects in multi-junction architectures. We have also illustrated the treatment of type-II superlattice IR detector absorber regions by the NRL BANDS™ software package, which employs an 8 band k·p model in conjunction with a Poisson solver. This was used to model quantum confined multi-layered media such as the type-II W-structured SL configuration. The WSL design has been implemented in high-performance graded-gap SL devices that approach the performance of state of the art HgCdTe LWIR photodetectors.

REFERENCES

[1] Barnham, K. W. J., and Duggan, G., "A new approach to high-efficiency multi-band-gap solar cells," J. Appl. Phys., 67(7), 3490-3493 (1990).

[2] Ekins-Daukes, N. J., Kawaguchi, K., and Zhang, J., "Strain-Balanced Criteria for Multiple Quantum Well Structures and Its Signature in X-ray Rocking Curves," Cryst. Growth Des., 2(4), 287-292 (2002).

[3] Wang, Y. P., Ma, S. J., Watanabe, K., Sugiyama, M., and Nakano, Y., "Management of highly-strained heterointerface in InGaAs/GaAsP strain-balanced superlattice for photovoltaic application," J. Cryst. Growth, 352(1), 194-198 (2012).

[4] Sugiyama, M., Wang, Y. P., Fujii, H., Sodabanlu, H., Wen, Y., Watanabe, K., and Nakano, Y., "Exploring the potential of quantum wells for efficiency enhancement in photovoltaic cells," Proc. SPIE. 8256, 82560D (2012).

[5] Adams, J. G. J., Browne, B. C., Ballard, I. M., Connolly, J. P., Chan, N. L. A., Ioannides, A., Elder, W., Stavrinou, P. N., Barnham, K. W. J., and Ekins-Daukes, N. J., "Recent results for single-junction and tandem quantum well solar cells," Prog. Photovolt: Res. Appl., 19(7), 865-877 (2011).

[6] Letay, G., and Bett, A. W., "EtaOpt - a program for calculating limiting efficiency and optimum bandgap structure for multi-bandgap solar cells and TPV cells," 17th IEEE European Photovoltaic Energy Conference. 178-181 (2001).

Downloaded From: http://proceedings.spiedigitallibrary.org/ on 04/01/2013 Terms of Use: http://spiedl.org/terms

[7] Browne, B., Ioannides, A., Connolly, J., Barnham, K., Roberts, J., Airey, R., Hill, G., Smekens, G., and Van Begin, J., "Tandem quantum well solar cells," IEEE Photovoltaic Specialists Conference. 565-569 (2008).

[8] Tibbits, T. N. D., Lumb, M. P., and Dobbin, A., "Quantum wells in multiple junction photovoltaics," Proc. SPIE. 7933, 793303 (2011).

[9] Gueymard, C. A., "Parameterized transmittance model for direct beam and circumsolar spectral irradiance," Sol. Energy, 71(5), 325-346 (2001).

[10] Lumb, M. P., Dobbin, A. L., Bushnell, D. B., Lee, K. H., and Tibbits, T. N. D., "Comparing The Energy Yield of (III-V) Multi-Junction Cells With Different Numbers Of Sub-Cells," Proc. CPV6. 1277, 299-302 (2010).

[11] Ma, S. J., Sodabanlu, H., Wang, Y., Watanabe, K., Sugiyama, M., and Nakano, Y., "InGaAs/GaAsP asymmetric quantum wells for enhancing carrier escape through resonant tunneling," 37th IEEE Photovoltaic Specialists Conference. (2011).

[12] Alemu, A., and Freundlich, A., "Improving photo-generated carrier escape in quantum well solar cells," Proc. SPIE. 8256, 82560B (2012).

[13] Lumb, M. P., Yakes, M. K., Gonzalez, M., Vurgaftman, I., Bailey, C. G., Hoheisel, R., and Walters, R. J., "Double quantum-well tunnel junctions with high peak tunnel currents and low absorption for InP multi-junction solar cells," Appl. Phys. Lett., 100(21), 213907 (2012).

[14] Dimroth, F., "High-efficiency solar cells from III-V compound semiconductors," Phys. Status Solidi C, 3, 373-379 (2006).

[15] Vinter, B., "Auger recombination in narrow-gap semiconductor superlattices," Phys. Rev. B., 66(4), 045324 (2002).

[16] Vurgaftman, I., Meyer, J. R., and Ram-Mohan, L. R., "Band parameters for III-V compound semiconductors and their alloys," J. Appl. Phys., 89(11), 5815-5875 (2001).

[17] Vurgaftman, I., Canedy, C. L., Jackson, E. M., Nolde, J. A., Affouda, C. A., Aifer, E. H., Meyer, J. R., Hood, A., Evans, A. J., and Tennant, W. T., "Analysis and performance of type-II superlattice infrared detectors," Opt. Engr., 50(6), 061007 (2011).

[18] Canedy, C. L., Boishin, G. I., Bewley, W. W., Kim, C. S., Vurgaftman, I., Kim, M., Lindle, J. R., Meyer, J. R., and Whitman, L. J., "Correlating growth conditions with photoluminescence and lasing properties of mid-IR antimonide type II "W" structures," J. Vac. Sci. Technol. B, 22(3), 1575-1579 (2004).

[19] Vurgaftman, I., Aifer, E. H., Canedy, C. L., Tischler, J. G., Meyer, J. R., Warner, J. H., Jackson, E. M., Hildebrandt, G., and Sullivan, G. J., "Graded band gap for dark-current suppression in long-wave infrared W-structured type-II superlattice photodiodes," Appl. Phys. Lett., 89(12), 121114 (2006).

[20] Aifer, E. H., Warner, J. H., Canedy, C. L., Vurgaftman, I., Jackson, E. M., Tischler, J. G., Meyer, J. R., Powell, S. P., Olver, K., and Tennant, W. E., "Shallow-Etch Mesa Isolation of Graded-Bandgap "W"-Structured Type II Superlattice Photodiodes," J. Electron. Mater., 39(7), 1070-1079 (2010).

Downloaded From: http://proceedings.spiedigitallibrary.org/ on 04/01/2013 Terms of Use: http://spiedl.org/terms

Analysis of GaAs Solar Cells at High MOCVD Growth Rates

Kenneth J. Schmieder*, Michael K. Yakes*, Christopher G. Bailey*, Ziggy Pulwin†, Matthew P. Lumb*‡, Louise C. Hirst*, María González*§, Seth M. Hubbard¶, Chris Ebert†, Robert J. Walters*

*U.S. Naval Research Laboratory, Washington, DC 20375 USA
†Veeco MOCVD, Somerset, NJ 08873 USA
‡George Washington University, Washington, DC 20052 USA
§Sotera Defense Solutions, Annapolis Junction, MD 20701 USA
¶NanoPower Research Labs, Rochester Institute of Technology, Rochester, NY 14623 USA

***Abstract*—Single junction GaAs solar cells grown by MOCVD are fabricated over a range of growth rates targeting up to 56 μm/hr in order to evaluate the effect on photovoltaic device performance. MOCVD recipe conditions are provided. Dopant incorporation efficiency is found to increase at high growth rates, potentially due to reduced Zn desorption as the time required to deposit a monolayer of GaAs is reduced. Device results are characterized by light and dark-IV as well as external quantum efficiency and verified against bulk minority carrier lifetime data from time-resolved photoluminescence. High growth rate solar cells degrade less than 4% relative to baseline devices with V_{oc} and J_{sc} losses of 1% and 3%, respectively. The comparison suggests that both bulk Shockley Read Hall (SRH) lifetime and surface recombination velocity (SRV) are affected by growth rate and contribute to a reduction in performance.**

***Index Terms*—III-V semiconductor materials, photovoltaic cells, semiconductor growth**

I. Introduction

III-V solar cells demonstrate the highest electrical conversion efficiency for both single and multijunction solar cells at 28.8% (one sun) and 44.4% (under concentration), respectively [1]. These continually improving electrical conversion achievements have been produced using a wide array of III-V material compositions and growth strategies. Still, efficiency improvements only account for one strategy toward reduced levelized cost of energy. Another pathway, with considerably less research, aims at the reduction of solar cell production costs by increasing epitaxial growth rate.

Accounting for some variation between different compound semiconductor foundries, standard commercial metal organic chemical vapor deposition (MOCVD) growth rates are presently around 14 μm/hr for GaAs. This facilitates the completion of GaAs solar cell structures in less than one hour with very high crystal quality. As growth rate is increased further, it is plausible that increased non-radiative recombination rates will begin to affect device performance. This is evident from time resolved photoluminescence (TRPL)-extracted minority carrier lifetime data for high growth rate GaAs by MOCVD, in which 10μm thick unintentionally doped double-heterostructures were found to have dramatically decreased lifetime at 56 μm/hr [2].

From $/Watt cost analysis, we estimate that if material quality can be improved such that devices are fabricated with less than 1% performance loss relative to baseline solar cells, a 56 μm/hr growth rate along with parallel studies to improve source utilization efficiency and reduce MOCVD tool overhead time can lead to a 74% reduction in single-junction III-V solar cell costs. In this manuscript we will explore the effect of increased growth rate on device performance. Preliminary results have shown a statistically insignificant change in device performance while doubling the rate in Veeco's MOCVD tool for both dual [3] and triple-junction solar cells [4]. In this report, flow rates will be quadrupled in order to target 56 μm/hr growth rates, believed to be well within the growth rate regime in which SRH recombination rates limit device performance, and results are provided from the epitaxial growth process to resulting material quality and photovoltaic device performance. High growth rate solar cells are shown to degrade less than 4% relative to baseline devices.

II. Epitaxial Growth

Solar cells are epitaxially grown using a Veeco K475 As/P MOCVD tool. The precursors used are trimethylgallium (TMGa), trimethylindium (TMIn), dimethylzinc (DMZn), arsine (AsH_3), phosphine (PH_3), and disilane (Si_2H_6). Growth rates targeted in this study are 14, 28, 42, and 56 μm/hr for Samples A, B, C, and D, respectively. The solar cells are grown at 635° C and target the structure detailed in Fig. 1, in which growth rate is varied for the device base and emitter while being maintained at standard rates for all other layers. Furthermore, the V/III flow ratio is maintained at 8.5, regardless of growth rate.

It was found that samples C and D had growth discrepancies which include a malfunctioning TMGa pressure controller and Zn incorporation complications. These errors provide insight into the challenges of high growth rate MOCVD and will be detailed in the following section.

In-situ normal incidence reflectivity from a laser source is utilized to verify experimental growth rate. Results of which indicate that growth rate scales at a 1:1 ratio with TMGa inlet flow rate at least through 28 μm/hr. This result is expected, as MOCVD growth under these standard process conditions is well-reported as mass transport limited by the group-III precursor [5]. However, the sampling rate of the in-situ reflectivity technique is not fast enough to provide accurate growth rate feedback above 28 μm/hr. For the initial dopant

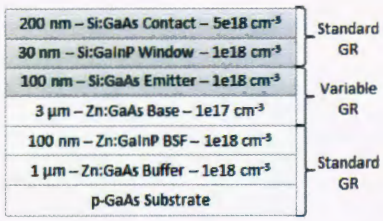

Fig. 1. Targeted structure of single-junction GaAs solar cell (all lattice-matched) processed for this report, identifying the layers in which growth rate (GR) is varied in this study

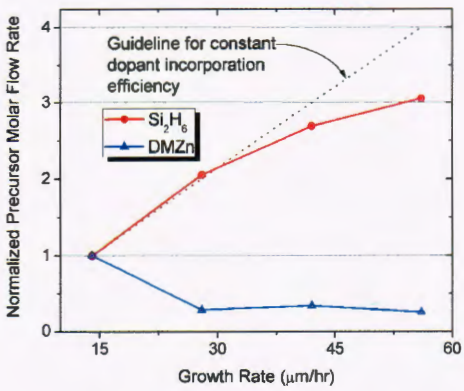

Fig. 2. Precursor flow rate, normalized to rates at 14 μm/hr, as a function of growth rate in order to achieve 1×10^{17} cm^{-3} Zn doping and 1×10^{18} cm^{-3} Si doping in GaAs. Guideline indicates a linear scale in flow rates.

calibration work, it was subsequently determined ex-situ that the growth rates do scale linearly through 56 μm/hr.

Dopant flow rates have been calibrated to target 1×10^{17} cm^{-3} and 1×10^{18} cm^{-3} for the base and emitter, respectively, at each growth rate. Electrically active dopant density is verified by electrochemical capacitance-voltage (ECV) profiling. Resultant dopant precursor flow rates, plotted in Fig. 2, suggest improved dopant incorporation efficiency at increased growth rates. The effect is particularly dramatic for DMZn, for which the flow rate must be reduced at increased growth rates in order to maintain 1×10^{17} cm^{-3} base doping. As initially postulated by Bass and Oliver [6], it is plausible that this improved DMZn incorporation efficiency is a function of a reduction in Zn desorption as the time required to deposit a monolayer of GaAs is reduced.

III. Photovoltaic Device Methodology & Results

All solar cells in this study have Ti/Au (20/200 nm) front and Cr/Au (10/200 nm) rear contacts. Devices are isolated to 5 mm x 5 mm dimensions using standard selective wet etch techniques. No anti-reflection (AR) coatings have been applied at this time. Devices are tested using an Oriel Light-IV setup simulating the AM1.5G spectrum calibrated with a GaAs reference cell.

Following fabrication, it was discovered that the TMGa pressure controller was faulty during growth of photovoltaic structures. This resulted in the base and emitter layers of

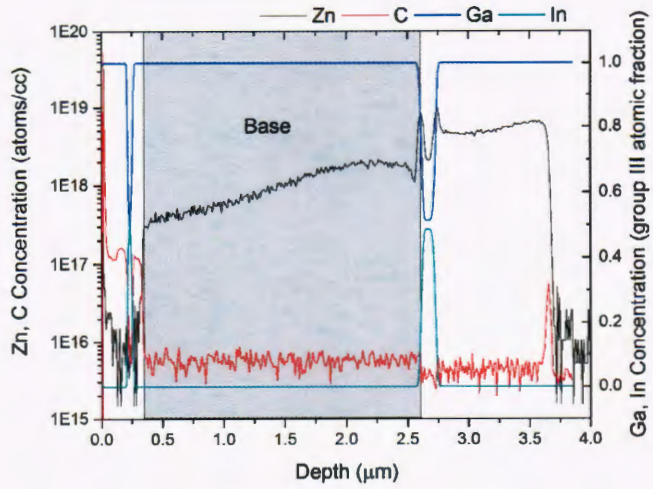

Fig. 3. SIMS depth profile for Sample D

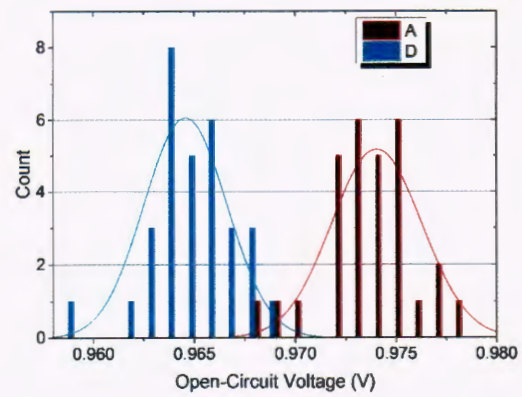

Fig. 4. Open-circuit voltage histogram for solar cells of samples A and D

samples C & D being grown at roughly 2/3 their targeted growth rates. Samples C & D therefore have thinner emitter and base widths than samples A & B. It was further discovered that excess Zn atoms from the BSF and buffer layer were incorporating in the base of higher growth rate samples, increasing the dopant density above the designed level and causing a Zn diffusion profile in the base. This can be visualized in the secondary ion mass spectrometry (SIMS) profile of Fig. 3.

The open-circuit voltage (V_{oc}) is evaluated as the primary metric of interest, as material quality fluctuations are expected to most severely impact the voltage. In Fig. 4, a V_{oc} histogram of all devices from samples A and D indicate that there is a loss incurred with one or multiple aspects of sample D. On average, the V_{oc} is reduced by 9 mV for sample D.

Due to the doping and base width growth discrepancies, it becomes difficult to unambiguously establish the cause of this performance degradation, but through evaluation of dark-IV (DIV) and utilization of advanced modeling capabilities, some differences will become evident. First, in order to fit the experimental DIV data, a numerical drift-diffusion solver,

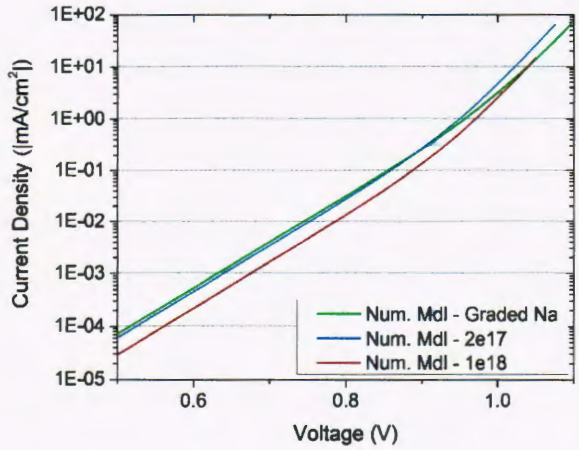

Fig. 5. Numerical drift-diffusion solver output for DIV of a graded and constant base dopant density

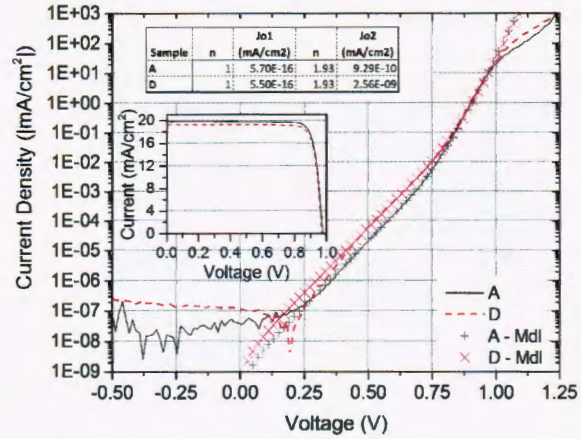

Sample	n	Jo1 (mA/cm2)	n	Jo2 (mA/cm2)
A	1	5.70E-16	1.93	9.29E-10
D	1	5.50E-16	1.93	2.56E-09

Fig. 6. Dark-IV plot for samples A and D along with simulated fits. Inset plot provides Light-IV results.

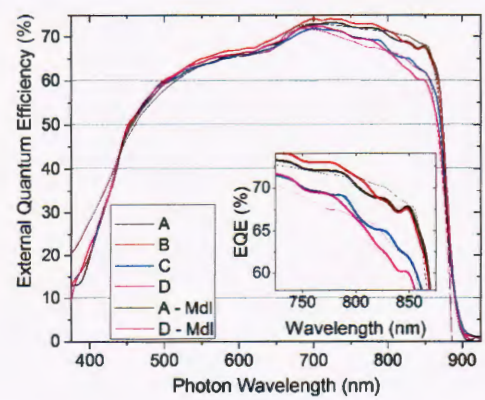

Fig. 7. External quantum efficiency at four growth rates (inset figure magnifies near-bandgap response)

part of the NRL Multibands®[7] software package, is used to evaluate whether the graded doping profile displayed in Fig. 3 can be approximated with a constant base doping level. It is advantageous if the structure can be simplified as this would allow fast and intuitive analytical evaluation [8] of the layer-by-layer structure including the impact of interface recombination (impact of SRV cannot be accounted for in the numerical solver at this time).

Fig. 5 shows the output of numerical simulation, in which constant base doping DIV simulations (SRH lifetime is held constant) are provided along with the graded doping output. It is apparent that the graded doping profile yields a more gradual slope change between n=2 and n=1 regions. The graded doping profile can be fit fairly well in the n=2 regime using the specified SRH lifetime and a lower (2e17 cm^{-3}) base dopant density. On the other hand, simulation of a higher constant base dopant density (1e18 cm^{-3}) is necessary in order to adequately fit the n=1 regime. Since the numerical simulation cannot account for SRV at this time, it is found that the experimental device is best fit in the analytical model with lower base dopant density and the inclusion of SRV. In doing so, one should keep in mind that the analytical simulation may overestimate the SRV value and underestimate the SRH recombination rate. The external quantum efficiency (EQE) is not expected to be noticeably changed by a graded vs. constant doping profile, since the diffusion length is much greater than the base width. We can therefore continue with the analytical simulation of DIV and EQE in order to compare extracted SRH lifetimes and SRV between samples A and D.

Examination of the recombination characteristics via DIV measurement is provided in Fig. 6. The n=1 regime dominates near V_{oc} for both devices, and suggests roughly identical J_{o1} values. The fact that these values are nearly equivalent despite the higher base doping in sample D suggests that the material quality is degraded in some capacity. The n=2 regime indicates a significant increase in saturation current density for sample D. The source of this change in J_{o2} is likely due to a 4X reduction to SRH lifetime. This agrees with TRPL studies of high growth rate undoped GaAs, in which SRH lifetimes were reduced with increasing growth rates [2].

The EQE is plotted for samples A, B, C, and D in Fig. 7. While long-wavelength response would generally be used to evaluate the impact of a change in diffusion lengths or SRV, due to the change in base width between samples, this analysis is not as straightforward. Instead, the diode parameters which were applied in Fig. 6 are used to simulate the EQE. The fit shows some error, more notably with sample D, but overall provides fair agreement across both DIV and EQE analyses. From this fit, it is found that the poor long-wavelength response is not only due to the shortened base width, but also a 1.67X increase in base/BSF SRV.

The extracted parameters used to compare samples A and D are summarized in Table I. While it cannot be determined from this study alone whether the changes in SRH lifetime and SRV are due to the increased growth rate or increased Zn impurity concentrations, subsequent studies are underway to clarify this.

An overall performance summary between samples A and

TABLE I
SAMPLES A AND D EXTRACTED PARAMETERS

Sample ID	J_{o1} (mA/cm^2)	J_{o2} (mA/cm^2)	SRH Lifetime (ns)	SRV_{Rear} (cm/s)
A	5.7e-16	9.3e-10	80	1.5e5
D	5.5e-16	2.6e-9	20	2.5e5

TABLE II
SINGLE-JUNCTION GAAS SOLAR CELL PERFORMANCE SUMMARY (AM1.5G)

	Sample ID	V_{oc} (mV)	J_{sc} (mA/cm^2)	FF (%)	η (%)
Avg.	A	974	18.2	85.0	15.1
	D	965	17.6	85.3	14.5
Hero	A	977	19.8	85.2	16.5
	D	968	19.2	85.6	15.9

D is provided in Table II. With regard to both hero cells and average performance, sample D solar cells are degraded by 9 mV (0.9%) and 0.6 mA/cm^2 (3%) relative to sample A. The difference in FF is likely a function of J_{sc} and not indicative of material quality differences. The FF would therefore be limited by series resistance, which is plausible when considering the non-ideal Ti/Au front contact composition and thickness. Regarding the control hero performance, the GaAs solar cell is presently unoptimized, as voltage is below expectations. The hero light IV curves are provided in the inset of Fig. 6.

IV. CONCLUSIONS

MOCVD growth of GaAs solar cells has been achieved targeting rates up to 56 μm/hr, a 4X increase over standard growth rates. Dopant incorporation efficiency is shown to increase with growth rate, most notably for DMZn, where the total precursor flow rate must be reduced relative to its 14 μm/hr value in order to maintain an equivalent dopant density. This effectively improves the dopant source efficiency, though also complicates the growth process of solar cell structures.

Solar cells have been fabricated for a range of growth rates. The results of which demonstrate a reduced V_{oc} and J_{sc} at highest growth rates, but not drastically so, as efficiency degrades less than 4% relative to control samples. Control devices are presently unoptimized and do not demonstrate the high-performance capable of single-junction GaAs. This may obscure the relative losses between different growth rates, as device performance is limited by other mechanisms than those of an ideal GaAs solar cell. A subsequent set of solar cells will target higher overall performance in order to evaluate this hypothesis.

Further studies will evaluate the defect mechanisms responsible for reduced performance as well as techniques to mitigate their impact. The successful completion of this goal, along with studies to improve source utilization efficiency and reduce MOCVD tool overhead, can result in a 74% reduction to single junction III-V solar cell costs and reduce MOCVD process cycle time from 42 to 15 minutes.

ACKNOWLEDGEMENT

This work was supported by the Office of Naval Research and was performed while K. J. Schmieder held National Research Council Research Associateship Awards at the U.S. Naval Research Laboratory

REFERENCES

[1] M. Green, K. Emery, Y. Hishikawa, W. Warta, and E. D. Dunlop, "Solar cell efficiency tables (version 43)," *Prog. Photovolt: Res. Appl.*, vol. 22, pp. 1–9, 2014.

[2] C. R. Haughn, K. J. Schmieder, J. M. Zide, A. Barnett, C. Ebert, R. Opila, and M. F. Doty, "Quantification of trap state densities in GaAs heterostructures grown at varying rates using intensity-dependent time resolved photoluminescence," *Appl. Phys. Lett.*, vol. 102, p. 182108, 2013.

[3] K. J. Schmieder, C. R. Haughn, Z. Pulwin, D. Dyer, J. Mutitu, M. Doty, C. Ebert, and A. Barnett, "Analysis of high growth rate MOCVD structures by solar cell device measurements," in *Proc. 37th IEEE Photovoltaic Specialists Conf.*, (Seattle), June 2011.

[4] C. Ebert, Z. Pulwin, D. Dyer, K. Schmieder, C. Haughn, L. Barclay, M. Doty, A. Barnett, and F. Lu, "High growth metal organic vapor phase epitaxy (MOVPE) for triple junction solar cells," in *Proc. 26th European Photovoltaic Solar Energy Conf.*, (Hamburg), Sept. 2011.

[5] G. B. Stringfellow, *Organometallic Vapor-Phase Epitaxy: Theory and Practice*. Academic Press, 1998.

[6] S. J. Bass and P. E. Oliver, "Controlled doping of gallium arsenide produced by vapour epitaxy, using trimethylgallium and arsine," in *Inst. Phys. Conf. Ser. No. 33b*, (St. Louis), pp. 1–10, 1976.

[7] M. P. Lumb, I. Vurgaftman, C. A. Affouda, J. R. Meyer, E. H. Aifer, and R. J. Walters, "Quantum wells and superlattices for III-V photovoltaics and photodetectors," in *Proc. SPIE 8471, Next Generation Nano Photonic and Cell Technologies for Solar Energy Conversion III*, (San Diego), Aug. 2012.

[8] M. P. Lumb, C. G. Bailey, J. G. J. Adams, G. Hillier, F. Tuminello, V. C. Elarde, and R. J. Walters, "Extending the one-dimensional Hovel model for coherent and incoherent back reflections in homojunction solar cells," *IEEE Journal of Quantum Electronics*, vol. 49, pp. 462–470, 2013.

Development of InGaAs Solar Cells for >44% Efficient Transfer-Printed Multi-junctions

Matthew P. Lumb[1,2], Matthew Meitl[3], John Wilson[3], Salvatore Bonafede[3], Scott Burroughs[3], David V. Forbes[4], Christopher G. Bailey[2], Nichole M. Hoven[4], María González[2,5], Raymond Hoheisel[1,2], Michael K. Yakes[2], Stephen J. Polly[4], Seth M. Hubbard[4] and Robert J. Walters[2]

[1]The George Washington University, Washington, DC 20007, USA
[2]Naval Research Laboratory, Washington, DC 20375, USA
[3]Semprius Inc., Durham, NC 27713, USA
[4]Rochester Institute of Technology, Rochester, NY 14623, USA
[5]Sotera Defense Solutions, Annapolis Junction, MD 20701, USA

Abstract – **Transfer-printing is a key enabling technology for the realization of ultra-high-efficiency, mechanically stacked III-V solar cells with low cost. In this work, we describe the development of InGaAs solar cells, designed to harvest long wavelength photons when stacked in tandem with a high efficiency InGaP/GaAs/InGaAsNSb triple junction solar cell. High performance InGaAs solar cells, grown on InP by MOCVD, were achieved through a combination of detailed modeling, material development and device characterization. The transfer printing apparatus of Semprius Inc. was used to create a four-terminal device with an uncertified conversion efficiency of 44.1% at 690 suns.**

I. INTRODUCTION

The current world-record solar cell is a wafer bonded, 2J (InGaP/GaAs) and 2J (InGaAsP/InGaAs) cell with an efficiency of 44.7% at a concentration factor of 297 suns [1]. The stacking of materials grown on two substrates capitalizes on the additional range of direct bandgaps afforded by the InP material system, enabling higher efficiencies than all GaAs or Ge-based cells. However, although extremely high efficiencies have been demonstrated in the laboratory and significant advances have been made to address the technological challenges of direct wafer bonding [2]; neither high temperature wafer-fusion techniques nor mechanical stacking using organic adhesives are currently mainstream manufacturing technologies to produce commercial solar cells.

An alternative approach is transfer-printing [3], a mature technology capable of producing mechanically stacked solar cells with high yield. Transfer printing also has significant advantages in manufacturability, combining reliable, repeatable and high-precision printing processes with the benefit of substrate reuse. This provides substantial cost savings over devices with non-reusable substrates, and allows an extremely broad palette of available III-V compounds for assembling high efficiency cells.

In this work we have designed, grown and optimized an InGaAs solar cell lattice-matched (LM) to InP, for use as a fourth junction when stacked with a commercial high efficiency InGaP/GaAs/InGaAsNSb 3J cell [4]. The resulting device is a four terminal, ultra high-efficiency solar cell designed for use in a high concentration PV module, with a conversion efficiency of 44.1% at 690 suns from very recent measurements.

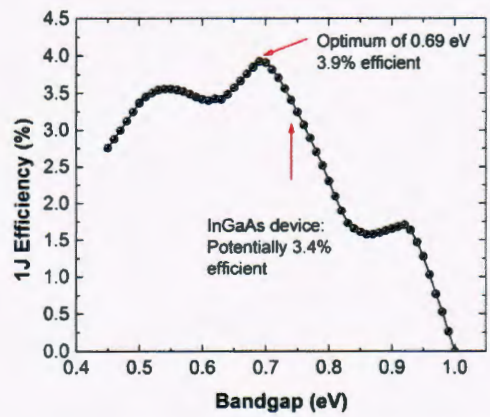

Fig. 1. Practical limiting efficiency of a single junction solar cell filtered by an InGaP/GaAs/InGaAsNSb 3J under 1000X AM1.5D illumination.

II. DESIGN AND GROWTH

The ideal bandgap of a 1J cell stacked with an 1.9 eV/1.4 eV/1.0 eV 3J cell is shown in figure 1 for 1000X AM1.5D illumination. In this calculation, a modified detailed-balance (MDB) model was used, where the standard assumptions of the model [5] were modified to give much more realistic efficiency estimates. The EQE of the cell filtered by the 3J was subject to a 10% optical loss, accounting for optical and carrier collection losses, the device was assumed to have a transparency of 5% and the saturation current density of the dark current, J_0, was assumed to be given by

$$J_0 = J_{0,r} e^{qV_d/kT} \quad [1]$$

Here J_{0r} is the radiative limit value and V_d is an empirical voltage drop of 120 mV, arising from imperfect carrier transport and non-radiative loss. At 1000 suns a 10% reduction in FF from the case without series resistance was assumed to reflect Ohmic losses. These empirical corrections were estimated based on comparisons with the figures of merit for very high performance solar cells in the literature, thus the model predictions represent a practical limit for device performance, rather than the fundamental limit given by detailed balance.

The optimum bottom cell bandgap for a four terminal (3J+1J) device is close to 0.69 eV. Recent work [6] demonstrated an efficiency of 43.9% by stacking the GaAs-based 3J with a Ge cell with a bandgap of 0.66eV, and the Ge cell produced approximately 1.8% efficiency at high concentration. This is lower than predicted by the MDB model, mainly due to the indirect bandgap of the material. However, InGaAs LM to InP is a direct bandgap semiconductor, and although the bandgap of 0.74 eV is slightly wider than optimal, a high quality InGaAs cell has the potential to outperform Ge.

The InGaAs solar cells in this study were n on p devices with InP window and back surface field (BSF) layers. InP has been shown to form high quality interfaces with InGaAs, therefore minimizing non-radiative interface recombination. A two micron highly doped InAlAs lateral conduction layer (LCL) was grown above the device, into which grid fingers were embedded. The InAlAs LCL layer was chosen due to the wide bandgap of 1.45 eV, minimizing the risk of any additional filtering of the InGaAs cell due to the LCL when in the stacked configuration. The device structure was designed using an analytical drift diffusion model built in to the NRL MultiBands® software package, described elsewhere [7], and calibrated using measured data for optical constants and carrier mobilities. The device design is summarized in table 1.

Three devices were grown by MOCVD with slightly different designs. InGaAs base doping values of 5×10^{17} cm^{-3} (sample A), 2.1×10^{17} cm^{-3} (sample B) and 1.1×10^{17} cm^{-3} (sample C) were grown to investigate the optimum value for base doping which ensures the diffusion length is sufficient to extract minority carrier efficiently yet maintains a large built in electric field across the junction.

Table I. Design for the InGaAs cell grown in this study.

Material	Description	Thickness (nm)	Doping (cm^{-3})
InP	cap	50	n = 1e18
InAlAs	LCL	2000	n= 4e18
InP	Window	50	n =1e18
InGaAs	Emitter	100	n = 1e18
InGaAs	Base	3000	p = var.
InP	BSF	50	p = 1.3e18
InP	Substrate	350 µm	p = 3e18

External quantum efficiency (EQE) measurements for the three designs are shown in figure 2. These measurements were performed on the bare cells, prior to mechanical stacking. The samples with lower base doping have an improved long wavelength response due to the longer minority carrier diffusion length in these devices. Simulating the devices using the drift-diffusion model (solid lines) revealed minority carrier diffusion lengths in the base region of 1.3 µm, 6.6 µm and 8.5 µm for the sample A, B and C respectively. The InAlAs thickness was varied in this fit to obtain good agreement in the fringe position due to interference effects in the LCL, which varied slightly device to device due to uncertainties in the growth rate.

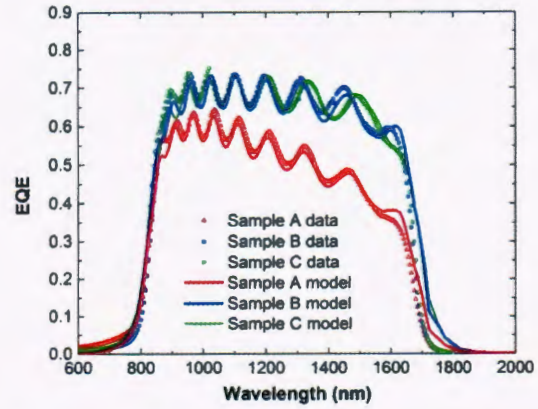

Fig. 2. Measured EQE for samples A, B and C (points) alongside modeled data using an analytical drift diffusion model.

III. TRANSFER PRINTING

The high efficiency 3J devices used in this work were grown by Solar Junction [4]. The devices were fabricated into

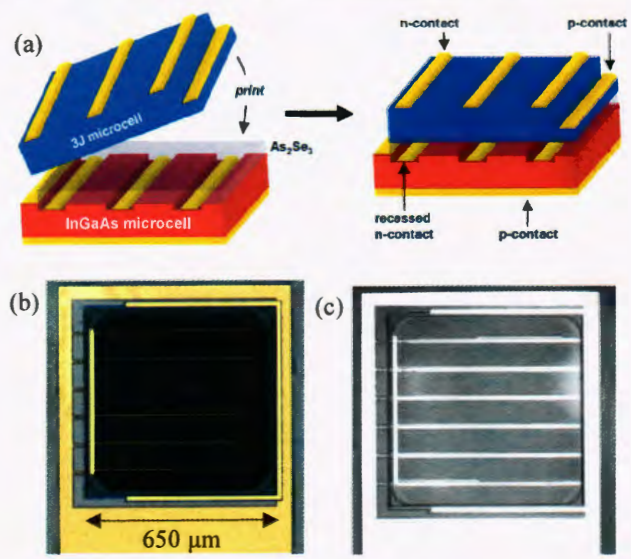

Fig. 3. (a) Schematic representation of the transfer printing process, adapted from reference [6]. (b) Optical microscope image of 3J stacked on InGaAs. (c) IR microscope image showing accurate alignment of grid fingers and a void free interface.

650×650 μm^2 chiplets and released from the growth substrate by wet chemical etching of an AlInP sacrificial etch layer at the base of the 3J stack. Contacting the back of the chiplets is done via a front-side contact to a thick GaAs lateral conduction layer at the base of the MJ stack, exposed during the mesa etch of the 3J device. The released 3J chiplets were transferred to the target wafer using a precisely controlled transfer printing procedure [8]. Contacts to the InGaAs solar cell were made via a planar Au/Zn/Au back metal on the p-InP wafer, and recessed grid fingers embedded in the InAlAs LCL layer. Reliable adhesion between the 3J chiplets and InGaAs cell was promoted using a spin-coated 25 nm layer of InterVia 8023-10 epoxy, which has a refractive index of ~1.61 at 632.8 nm. The calculated reflectivity at the interface of GaAs/$In_{0.52}Al_{0.48}As$ using a 25 nm epoxy interface layer is shown in figure 4(a), and results in <3% optical loss over the range of InGaAs spectral response.

Any voids or particles on the surfaces can disrupt the contact quality between the surfaces and introduce significant interface reflections. However, successful printing was achieved with these samples and a well aligned, stacked cell free of voids is shown in the optical and IR microscope images in figure 3(b). The precise nature of the transfer printing technique allows the grid fingers of the metallization patterns to be aligned, minimizing the shading losses.

A recent innovation [6] for achieving reliable adhesion of the printed cells is to use a chalcogenide glass layer, As_2Se_3. This material is transparent in the infrared and refractive-index matched to the cells, therefore giving excellent optical performance. The material also serves as an electrically isolating and thermally conductive interface layer in these stacks. Figure 3(a) shows a schematic representation of the transfer printing procedure using the chalcogenide glass. Deposition of the As_2Se_3 film is compatible with conventional sol-gel processes and results in high-yield and robust stacked cells. Further stacking experiments using this interfacial technology are planned for future experiments.

IV. LIGHT-IV MEASUREMENTS

The sample with the highest performance was sample C, which has the lowest base doping concentration. After printing the 3J cell on to this device, the illuminated IV characteristics of the InGaAs cell were measured using a 1342 nm Nd:YVO_4 laser. The 1 sun value of the cell after stacking was found by integrating the EQE of the InGaAs cell filtered by the 3J with the AM1.5D spectrum. The EQE of the InGaAs cell with and without the 3J printed is shown in figure 4(b) for structure C. The EQE of the stacked cell is attenuated at wavelengths short than about 1300 nm due to the absorption in the GaAs-based MJ. This gives a value of 7.14 mA/cm^2. The LIV curve of the InGaAs cell at an illumination level equivalent to 690 suns is shown in figure 5. The efficiency of the InGaAs cell under this illumination is 2.1%. However, the FF of the InGaAs device after stacking was lower than expected, and further process

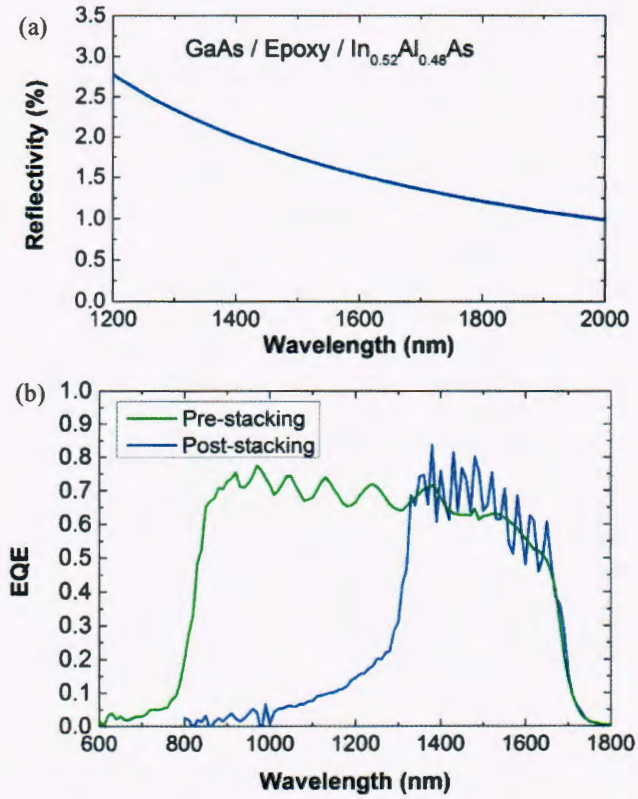

Fig. 4. (a) The calculated reflectivity at the GaAs/InAlAs interface assuming a 25 nm epoxy interconnecting layer. (b) Measured EQE of the InGaAs device before and after stacking with the high-efficiency 3J device.

optimization in the metallization recipe and LCL design are expected to surpass this efficiency value.

The measured LIV characteristics of the InGaP/GaAs/InGaAsNSb 3J is also shown in figure 5. This data is taken from an identical device characterized using simulated AM1.5D illumination, presented in reference [6]. The data presented is at slightly lower concentration of ~640 suns, but gives a comparable efficiency figure to the device at 690 suns. At this time, data under simulated AM1.5D conditions for the actual 3J printed are ongoing, however the high uniformity of the 3J devices means a reliable estimate can be made from the identical device already characterized. The efficiency of this device is 42.0%, giving a combined efficiency of 44.1%. This is presently unconfirmed by a certified test facility, and certification of InGaAs+3J stacked devices is planned in the near future. Improvements in the contacting and current spreading properties of the InGaAs cell are expected to yield a stacked device with a world record efficiency, and open up a pathway to new concepts in ultra-high-efficiency, transfer-printed MJ solar cells.

V. CONCLUSION

In this paper we have presented recent results of stacking high-efficiency, commercially available 3J solar cells with

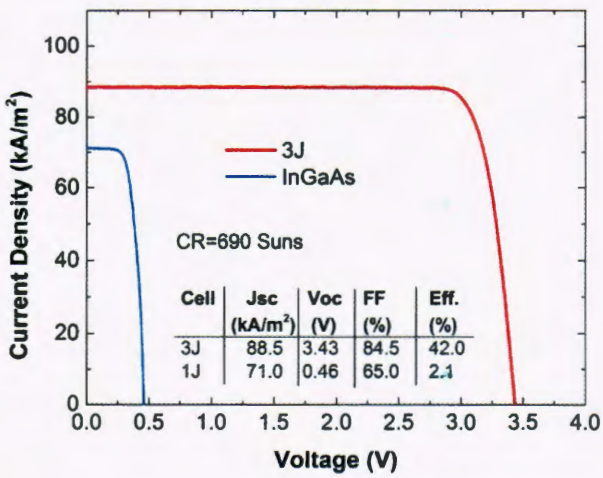

Fig. 4. Illuminated IV curves at 560 suns for the InGaAs and 3J cells. Illumination for the InGaAs cell was a 1342 nm laser, with CR determined from the J_{sc} under 1 sun AM1.5D illumination.

InGaAs solar cells using a transfer-printing technique. Three different InGaAs designs were evaluated with varying base doping and the minority carrier transport properties were ascertained by comparison to a detailed solar cell model. The highest efficiency design was used to fabricate four terminal, mechanically stacked solar cells with a 25 nm epoxy interconnect layer, giving low optical loss. A J_{sc} of 7.14 mA/cm^2 was achieved post-stacking, which gave an efficiency of 2.1% at 690 suns, and a combined efficiency of 44.1% with the high efficiency 3J device.

ACKNOWLEDGEMENTS

The authors would like to acknowledge Solar Junction for providing the high efficiency 3J devices and Xing Sheng and the group of John Rogers at University of Illinois, Urbana-Champaign for help in the processing of these devices.

REFERERNCES

[1] F. Dimroth, M. Grave, P. Beutel, U. Fiedeler, C. Karcher, T. N. D. Tibbits, E. Oliva, G. Siefer, M. Schachtner, A. Wekkeli, A. W. Bett, R. Krause, M. Piccin, N. Blanc, C. Drazek, E. Guiot, B. Ghyselen, T. Salvetat, A. Tauzin, T. Signamarcheix, A. Dobrich, T. Hannappel, and K. Schwarzburg, "Wafer bonded four-junction GaInP/GaAs//GaInAsP/GaInAs concentrator solar cells with 44.7% efficiency," *Progress in Photovoltaics: Research and Applications,* pp. n/a-n/a, 2014.

[2] H. Moriceau, F. Rieutord, F. Fournel, Y. Le Tiec, L. Di Cioccio, C. Morales, A. Charvet, and C. Deguet, "Overview of recent direct wafer bonding advances and applications," *Advances in Natural Sciences: Nanoscience and Nanotechnology,* vol. 1, p. 043004, 2010.

[3] A. Carlson, A. M. Bowen, Y. Huang, R. G. Nuzzo, and J. A. Rogers, "Transfer Printing Techniques for Materials Assembly and Micro/Nanodevice Fabrication," *Advanced Materials,* vol. 24, pp. 5284-5318, 2012.

[4] D. Derkacs, R. Jones-Albertus, F. Suarez, and O. Fidaner, "Lattice-matched multijunction solar cells employing a 1 eV GaInNAsSb bottom cell," *Journal of Photonics for Energy,* vol. 2, pp. 021805-1, 2012.

[5] G. Letay and A. W. Bett, "EtaOpt - a program for calculating limiting efficiency and optimum bandgap structure for multi-bandgap solar cells and TPV cells," in *17th European Photovoltaic Energy Conference*, Munich, 2001, pp. 178-181.

[6] X. Sheng, C. Bower, S. Bonafede, J. W. Wilson, B. Fisher, M. Meitl, H. Yuen, S. Wang, L. Shen, S. Burroughs, and J. A. Rogers, "Printing-based assembly of quadruple junction, four-terminal microscale solar cells and their use in modules with high operating efficiencies," *Submitted to Nature Materials,* 2013.

[7] M. P. Lumb, C. G. Bailey, J. G. J. Adams, G. Hillier, F. Tuminello, V. C. Elarde, and R. J. Walters, "Extending the One-Dimensional Hovel Model for Coherent and Incoherent Back Reflections in Homojunction Solar Cells," *IEEE Journal of Quantum Electronics,* vol. 49, pp. 462-470, 2013.

[8] M. A. Meitl, Z.-T. Zhu, V. Kumar, K. J. Lee, X. Feng, Y. Y. Huang, I. Adesida, R. G. Nuzzo, and J. A. Rogers, "Transfer printing by kinetic control of adhesion to an elastomeric stamp," *Nat Mater,* vol. 5, pp. 33-38, 2006.